

The fate of poor man's Majoranas in the long Kitaev chain limit

Melina Luethi^{†,1}, Henry F. Legg^{†,1,*}, Daniel Loss¹ and Jelena Klinovaja¹

¹*Department of Physics, University of Basel, Klingelbergstrasse 82, CH-4056 Basel, Switzerland*

[†]*These authors contributed equally to this work.*

(Dated: August 20, 2024)

A minimal Kitaev chain, consisting of two quantum dots connected via a superconductor, can host highly localized near-zero-energy states, known as poor man's Majoranas (PMMs). These states have been proposed as promising candidates to study Majorana bound states (MBSs) in a highly tunable setup. However, it is unclear whether and how PMMs observed in real systems are actually connected to the topological phase of the full Kitaev chain. Here, we study PMMs using a microscopic model and show that, in the long chain limit, not all PMMs are related to topological states. Rather, in long chains, some PMMs evolve into trivial highly localized low-energy states. We provide an analytical explanation for the occurrence of these states and show that there is no clear conductance signature that is able to distinguish PMMs that evolve into true topological states from PMMs that evolve into trivial states.

Majorana bound states (MBSs) are quasiparticles that emerge at the boundaries or in vortices of topological superconductors [1] and, due to their non-Abelian exchange statistics [2], have been proposed as candidates to store and manipulate quantum information in a fault-tolerant way [3–5]. They were prominently described using the Kitaev chain [1], a simple spinless minimal model relying on p -wave superconductivity. Nanowires with strong spin-orbit interaction (SOI) proximitized by superconductors have in recent years been prominent systems to realize an effective Kitaev chain [6–12]. However, disorder has hindered the conclusive observation of MBSs in these heterostructures since disorder can result in signatures that mimic MBSs [13–33]. Due to the issues with disorder in nanowires, realizing an effective Kitaev chain as an array of quantum dots (QDs) has been proposed as an alternative platform to host MBSs with a high degree of tunability [34–73]. In these proposals, the QDs are separated by superconducting sections, which couple the QDs through elastic cotunneling (ECT) and crossed Andreev reflection (CAR) [74–80]. In such setups, an inhomogeneous magnetic field or SOI can enable effective p -wave superconductivity using a conventional s -wave superconductor [34, 35].

It has been shown that a fully spin-polarized model consisting of only two QDs with a superconductor transmitting ECT and CAR between the QDs is sufficient to obtain states similar to MBSs [35]. These states share most of their properties of the MBSs found in long Kitaev chains, i.e., they are at zero energy, separated from the excited states by a finite gap, and have non-Abelian exchange statistics. However, they exist only at finely tuned points of parameter space, called “sweet spots”, and therefore they lack topological protection. Due to this lack of protection MBSs in minimal Kitaev chains are often called “poor man's Majoranas” (PMMs).

Recent demonstrations of control over the strength of ECT and CAR [41, 81–86] have spurred great interest in PMMs. Although originally derived using the spinless

Kitaev chain, PMMs have also been studied in spinful models [36, 40, 41, 43, 46–49, 51, 54–56, 59–61, 63, 65–67, 71–73]. It was shown in Ref. 73 that sweet spots with perfectly localized zero-energy PMMs can exist in an idealized spinful model, however, reaching these sweet spots requires complete control over many degrees of freedom. In more realistic models and experiments such control is not possible and so only “imperfect PMMs” are possible, i.e., states that are close to zero energy and highly – but not perfectly – localized.

In recent experiments, conductance signatures associated with PMMs have been found [42, 47, 52, 57, 60]. Whilst theoretical proposals for braiding PMMs also exist [49, 53, 59], these have not yet been demonstrated. Given that only imperfect PMMs are possible in realistic setups and experiments, it is important to clarify whether these states are actually connected to topological states in the Kitaev chain, or if they are simply well-localized near-zero-energy states that evolve into trivial states in the long chain limit.

In this Letter, we demonstrate that imperfect PMMs in a microscopic model of the minimal Kitaev chain are not necessarily connected to topological MBSs in the long chain limit. We explain analytically the origin of these imperfect PMMs and demonstrate that there is no clear conductance signature in a minimal Kitaev chain that can distinguish PMMs that evolve into true MBSs from PMMs that evolve into highly localized trivial states.

Model: To model a minimal Kitaev chain microscopically we consider a system of three QDs, see Fig. 1(a), based on the model introduced in Ref. 40. The left and right QDs, modelling the two sites of a minimal Kitaev chain, have chemical potentials μ_L and μ_R , respectively (if not stated otherwise, we will assume $\mu_L = \mu_R \equiv \mu$), a Zeeman energy Δ_Z , and on-site Coulomb repulsion U . The middle QD is proximitized by a superconductor and models an Andreev bound state that effectively transmits ECT and CAR between the outer QDs [40, 41, 46, 47, 51, 63, 71, 87]. The middle QD also

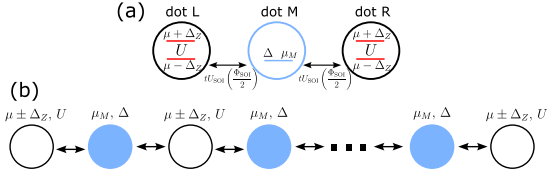


FIG. 1. **Microscopic model of a minimal Kitaev chain and the long chain limit.** (a): Minimal Kitaev chain, consisting of three QDs. The left and right QDs, representing two Kitaev sites, have a chemical potential μ , Zeeman energy Δ_Z , and on-site Coulomb interaction U . The middle QD M has a superconducting pairing potential Δ and, due to the screening by the superconductor, we assume no Zeeman energy or Coulomb interaction. This middle QD models an Andreev bound state (ABS) that transmits the effective couplings between the two outer QDs. The hopping amplitude is t and $U_{\text{SOI}}(\Phi_{\text{SOI}}/2)$ characterizes the SOI. (b): Long chain limit. Normal QDs are white, they are equivalent to the QDs L and R in (a) and each represents one normal site. The QDs with a pairing potential are blue and they are equivalent to the QD M in (a).

causes local Andreev reflection (LAR) and renormalizes other parameters of the outer QDs [73]. This middle dot has a superconducting pairing potential Δ and a chemical potential μ_M . Due to screening by the superconductor we will assume that the middle QD has no Zeeman energy and no Coulomb repulsion. We note, however, that it has been shown in Ref. 40 that, even without this assumption for the middle QD, PMMs persist in the system studied. The hopping between the QDs is determined by the hopping amplitude t and the SOI angle Φ_{SOI} . The Hamiltonian describing the system is given by

$$H = \sum_{j=L,R} \left[\sum_{\sigma=\uparrow,\downarrow} (\mu_j + \sigma\Delta_Z) n_{j,\sigma} + U n_{j,\uparrow} n_{j,\downarrow} \right] + \sum_{\sigma=\uparrow,\downarrow} \mu_M c_{\sigma}^{\dagger} c_{\sigma} + \Delta (c_{\uparrow}^{\dagger} c_{\downarrow}^{\dagger} + c_{\downarrow} c_{\uparrow}) + t \sum_{\sigma,\sigma'=\uparrow,\downarrow} \left[U_{\text{SOI}} \left(\frac{\Phi_{\text{SOI}}}{2} \right)_{\sigma\sigma'} (c_{\sigma}^{\dagger} d_{1,\sigma'} + d_{2,\sigma}^{\dagger} c_{\sigma'}) + \text{H.c.} \right], \quad (1)$$

where $n_{j,\sigma} = d_{j,\sigma}^{\dagger} d_{j,\sigma}$, $d_{j,\sigma}^{\dagger}$ (c_{σ}^{\dagger}) creates a particle on dot $j \in \{L, R\}$ (the middle QD M), μ_M is the chemical potential on the middle QD, and the notation $\sigma\Delta_Z$ means $+\Delta_Z$ for $\sigma=\uparrow$ and $-\Delta_Z$ for $\sigma=\downarrow$. The chemical potentials are measured with respect to the chemical potential of the superconductor. Assuming that SOI is perpendicular to the magnetic field, the SOI matrix is given by

$$U_{\text{SOI}} \left(\frac{\Phi_{\text{SOI}}}{2} \right) = \cos \left(\frac{\Phi_{\text{SOI}}}{2} \right) + i \sin \left(\frac{\Phi_{\text{SOI}}}{2} \right) \sigma_y, \quad (2)$$

where σ_y is the second Pauli matrix. We will use the second quantized form and, if $U = 0$, also the BdG form of the Hamiltonian given in Eq. (1) for the calculations in this work, see SM [88].

The Hamiltonian given in Eq. (1) conserves the total particle number parity. Therefore, the second quantized Hamiltonian is block diagonal. We label the Hamiltonian coupling states with an even (odd) particle number as H_{even} (H_{odd}), its eigenstates as $|\Psi_a^{\text{even}}\rangle$ ($|\Psi_a^{\text{odd}}\rangle$) and the corresponding eigenvalues as E_a^{even} (E_a^{odd}), where a numbers the eigenstates and eigenvalues such that $E_0^{\text{even}} \leq E_1^{\text{even}} \leq \dots$ ($E_0^{\text{odd}} \leq E_1^{\text{odd}} \leq \dots$). We introduce the energy difference [35]

$$\Delta E = E_0^{\text{even}} - E_0^{\text{odd}}, \quad (3)$$

the charge difference on dot $j \in \{L, R\}$ [40]

$$\Delta Q_j = \sum_{\sigma=\uparrow,\downarrow} (\langle \Psi_0^{\text{even}} | n_{j,\sigma} | \Psi_0^{\text{even}} \rangle - \langle \Psi_0^{\text{odd}} | n_{j,\sigma} | \Psi_0^{\text{odd}} \rangle), \quad (4)$$

the Majorana polarization (MP) on dot $j \in \{L, R\}$ [40]

$$M_j = \frac{\left| \sum_{\sigma=\uparrow,\downarrow} (w_{+,\sigma}^2 - w_{-,\sigma}^2) \right|}{\sum_{\sigma=\uparrow,\downarrow} (w_{+,\sigma}^2 + w_{-,\sigma}^2)}, \quad (5a)$$

$$w_{\pm,\sigma} = \langle \Psi_0^{\text{odd}} | (d_{j,\sigma} \pm d_{j,\sigma}^{\dagger}) | \Psi_0^{\text{even}} \rangle, \quad (5b)$$

and the excitation gap [73]

$$E_{\text{ex}} = \min \{ E_1^{\text{even}} - E_0^{\text{even}}, E_1^{\text{odd}} - E_0^{\text{odd}} \}. \quad (6)$$

Region of threshold: A sweet spot is a point in parameter space that fulfills $\Delta E = 0$, $\Delta Q_L = \Delta Q_R = 0$, $M_L = M_R = 1$, and $E_{\text{ex}} > 0$. The corresponding “perfect PMMs” to these sweet spots are completely localized and at zero energy. It was shown in Ref. [73] that, for the microscopic Hamiltonian of a minimal Kitaev chain in Eq. (1), no perfect sweet spots could be found. Instead, the notion of a “region of threshold” (ROT) was introduced. It is a region of parameter space where the PMM conditions are *approximately* realized, i.e.,

$$\begin{aligned} & |\Delta E| < \Delta E_{\text{th}} \text{ and } E_{\text{ex}} > E_{\text{ex,th}} \\ & \text{and } |\Delta Q_L| < \Delta Q_{\text{th}} \text{ and } |\Delta Q_R| < \Delta Q_{\text{th}} \\ & \text{and } M_L > 1 - M_{\text{th}} \text{ and } M_R > 1 - M_{\text{th}}, \end{aligned} \quad (7)$$

where ΔE_{th} , $E_{\text{ex,th}}$, ΔQ_{th} , and M_{th} are threshold values which need to be chosen. The corresponding “imperfect PMMs” have energies near zero and are highly – but not perfectly – localized. This highlights, however, that it is necessary to have a degree of arbitrariness in the definition of a PMMs in realistic systems that will always depend on the threshold values chosen in Eq. (7).

Connection to topology: Although the requirement to define a ROT creates some ambiguity, it is often implicitly assumed that imperfect PMMs in more realistic microscopic models, such as that shown in Fig. 1(a), will still evolve into topological MBSSs in the long chain limit, i.e., in the system shown in Fig. 1(b). In the following, we will demonstrate that this is not necessarily the case

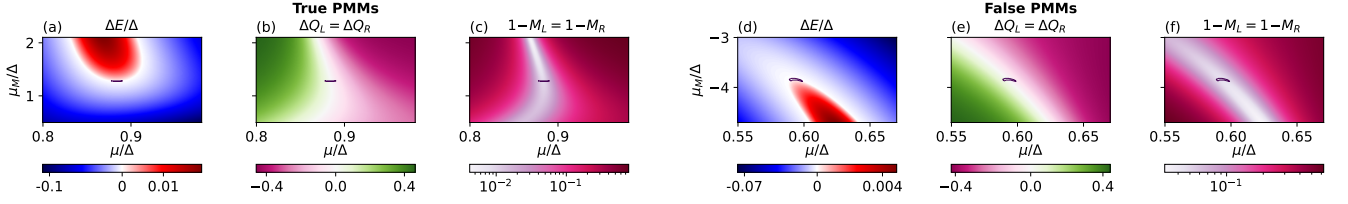


FIG. 2. **Quality measures for true PMMs versus false PMMs.** Energy difference ΔE [(a) and (d)], charge difference ΔQ_j [(b) and (e)], and the Majorana polarisation M_j [(c) and (f)] for two parameter sets. The area circled in black is the ROT. Both sets of parameters lead to qualitatively equal results, and both lead to a ROT with highly localized near-zero-energy states, i.e., PMMs. However, only (a)-(c) are connected to true MBSSs in the long chain limit, whereas (d)-(f) are connected to trivial states in the long chain limit, see Fig. 3. The parameters for (a)-(c) are $t/\Delta = 0.42$, $\Phi_{\text{SOI}} = 0.26\pi$, $U = 0$, and $\Delta_Z/\Delta = 0.8$. The largest excitation gap in the ROT is $E_{\text{ex}}/\Delta = 0.103$. The parameters for (d)-(f) are $t/\Delta = 0.99$, $\Phi_{\text{SOI}} = 0.44\pi$, $U = 0$, and $\Delta_Z/\Delta = 0.8$. The largest excitation gap in the ROT is $E_{\text{ex}}/\Delta = 0.084$. The ROT threshold values for all panels are $\Delta E_{\text{th}}/\Delta = 10^{-4}$, $\Delta Q_{\text{th}} = 0.05$, and $M_{\text{th}} = 0.05$.

and show that none of the previously used experimental signatures for PMMs can clearly distinguish between PMMs that would evolve into topological states, from those that evolve into highly localized trivial states.

For instance, in Fig. 2, we consider two sets of parameters, both result in a ROT and therefore correspond to highly localized imperfect PMMs. In the minimal Kitaev chain limit, the ground state energy difference ΔE , the charge difference ΔQ_j , and the MP M_j (all shown in Fig. 2) give qualitatively similar results for both parameter sets. However, in the long chain limit, we observe that only one of the two parameter sets actually results in MBSSs, whereas the other parameter set results in states that are highly localized but trivial, see Fig. 3. We verify this in the infinite chain limit using the topological invariant Q_{Z_2} , see SM [88]. If $Q_{Z_2} = 1$ ($Q_{Z_2} = -1$), the system is trivial (topological). In the trivial case, the highly localized state we observe in the ROT is associated with two doubly degenerate states that split from the bulk states and cross zero energy in the long chain limit. We emphasize that these states become degenerate only in the long chain limit, i.e., in short chains $E_{\text{ex}} > 0$. We call these states that appear in a ROT, but that are not connected to topological states in the long chain limit “false PMMs”. We note that we set $U = 0$ for the examples shown here, however, false PMMs also exist for finite U , see SM [88].

Conductance signatures: Zero-bias conductance is often used as a signature to search for PMMs in a minimal Kitaev chain [42, 47, 52, 57, 60]. We use the Python package Kwant [89] to calculate the conductance $G_{\alpha\beta} = dI_{\alpha}/dV_{\beta}$, attaching leads to the two outer QDs and introducing the coupling t_l between the QDs and the leads. Varying μ_L and μ_R , for different values of μ_M , we expect a clear signature in the ROT associated with PMMs. Within the ROT, there is a crossing of the conductance at $\mu_L = \mu_R$. As μ_M is varied away from its value in the ROT, the zero-energy conductance exhibits an anti-crossing and the non-local conductance changes its sign [40, 42, 47, 60]. We find this signature for both

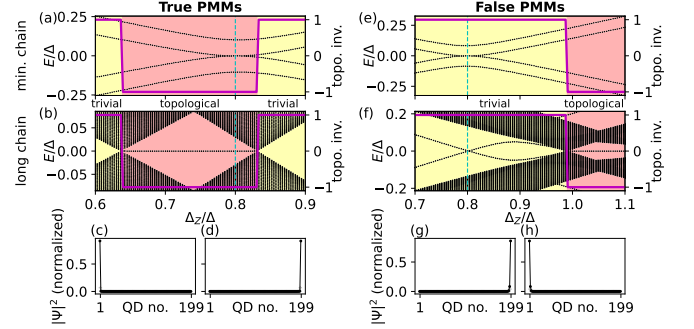


FIG. 3. **True and false PMMs in the long chain limit.** Energy spectrum E (black dots) as a function of the Zeeman energy Δ_Z for the minimal chain [(a) and (e)] and in the long chain limit [(b) and (f)]. The magenta line indicates the topological invariant, calculated in the infinite chain limit, see SM [88]. A red (yellow) background in the spectrum indicates that the system is topological (trivial). (c) and (d): Probability density of the two zero-energy states at $\Delta_Z/\Delta = 0.8$ from (b). The weight on the normal (superconducting) QDs are indicated by black dots (gray crosses). These states are MBSSs. (g) and (h): Probability density of two zero-energy states at $\Delta_Z/\Delta = 0.8$ in (f). Although these states are at zero-energy and mainly localized on the first and last QD, they are trivial and not related to MBSSs. Hence, although in the minimal chain [(a) and (e)], both sets of parameters result in qualitatively similar results, only one of the parameter sets is connected to a topological state in the long chain limit. The parameters for (a)-(d) are as for (a)-(c) in Fig. 2 with $\mu/\Delta = 0.884$ and $\mu_M/\Delta = 1.275$. The parameters for (e)-(h) are as for (d)-(f) in Fig. 2 with $\mu/\Delta = 0.593$ and $\mu_M/\Delta = -3.836$. The long chain consists of 100 normal QDs and 99 QDs with a pairing potential.

parameter sets, see Fig. 4. This means that zero-energy conductance cannot clearly distinguish false PMMs from true PMMs, i.e., those that evolve into topological states in the long chain limit.

Another signature which has been used to identify PMMs is the finite energy conductance when tuning the chemical potential of only one, e.g. the left, QD away

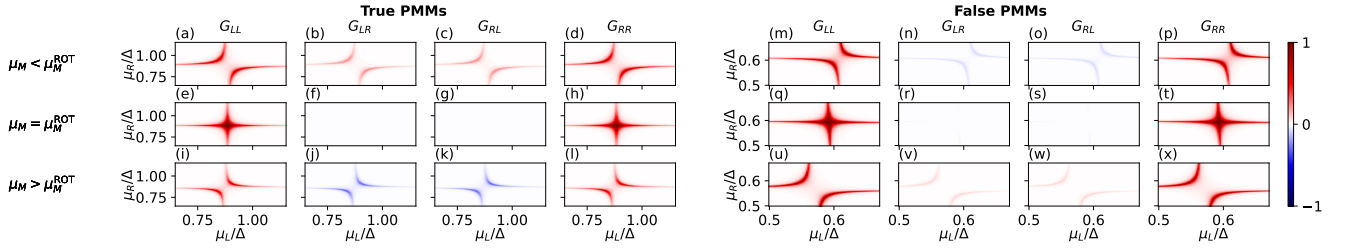


FIG. 4. **Zero-bias conductance signatures of true PMMs versus false PMMs.** Normalized zero-energy conductance G_{LL} [(a), (e), (i), (m), (q), and (u)], G_{LR} [(b), (f), (j), (n), (r), and (v)], G_{RL} [panels (c), (g), (k), (o), (s), and (w)], and G_{RR} [(d), (h), (l), (p), (t), and (x)], as μ_L and μ_R are varied independently, for different values of μ_M . For each setup all conductance values are normalized with respect to the maximum value. In (a)-(l) the same parameters as for (a)-(c) in Fig. 2 are used, with $\mu_M/\Delta = 0.975$ for (a)-(d), $\mu_M/\Delta = 1.275$ (corresponding to the value for the ROT) for (e)-(h), and $\mu_M/\Delta = 1.975$ for (i)-(l). The coupling to the leads is $t_l/\Delta = 0.005$. In (m)-(x) the same parameters as for (d)-(f) in Fig. 2 are used, with $\mu_M/\Delta = -4.236$ for (m)-(p), $\mu_M/\Delta = -3.836$ (corresponding to the value for the ROT) for (q)-(t), and $\mu_M/\Delta = -3.336$ for (u)-(x). The coupling amplitude to the leads is $t_l/\Delta = 0.001$. Although both parameter sets give qualitatively similar results, only the parameters for (a)-(l) are related to true MBSs in the long chain limit, whereas (m)-(x) are related to trivial states.

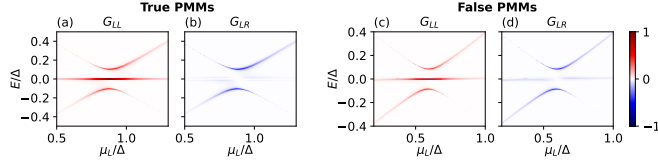


FIG. 5. **Finite-energy conductance of true PMMs versus false PMMs.** Normalized conductance at energy E , as the chemical potential of the left QD, μ_L , is varied, while the chemical potential of the right QD remains at its value in the ROT. (a) and (c) show the local conductance G_{LL} , (b) and (d) show the nonlocal conductance G_{LR} . For each setup all conductance values are normalized with respect to the maximum value. The parameters for (a) and (b) are the same as for (a)-(c) in Fig. 2, with $t_l/\Delta = 0.01$. The parameters for (c) and (d) are the same as for (d)-(f) in Fig. 2, with $t_l/\Delta = 0.006$. Both sets of parameters result in qualitatively similar results, but only (a) and (b) are related to true MBSs in the long chain limit, whereas (c) and (d) are related to trivial states in a long chain.

from the ROT [42, 56, 60]. However, we again find that there is no clear qualitative difference in this signature between a false and a true PMM, see Fig. 5. In the SM [88], we also show finite energy conductance results when both QDs are tuned away from the ROT. This, too, is inadequate to distinguish false from true PMMs.

Origin of false PMMs: As shown in Fig. 3, in the long chain limit, the false PMMs discussed here are related to degenerate energy levels that are split from the bulk states. These false PMMs can be associated with localized zero-energy states in a system consisting of only two QDs, see SM [88], in particular, these false PMMs arise because the first and last normal QDs of a chain couple directly to only one superconducting QD, but the bulk normal QDs couple directly to two superconducting QDs.

Using the microscopic model defined in Eq. (1) we have found many examples of false PMMs, see SM [88]. Most

of these false PMMs are related to trivial zero-energy states in the long chain limit, which was our focus here. However, some false PMMs do not relate to zero-energy states in the long chain limit [88]. Furthermore, it might seem that starting and ending the long chain with superconducting QDs makes the outer normal QDs equivalent to the bulk normal QDs. This, however, is not the case, and we still find that false PMMs exist in this modified model, see SM [88].

Conclusion: We found that signatures so far associated with PMMs can also originate from “false PMMs”, which are states that are near-zero-energy and highly localized in the minimal chain, but do not evolve into topological states in the long chain limit. Although we focussed on minimal chains here, we find also that short uniform chains consisting of a few QDs [52] can also host false PMMs, but with a reduced excitation gap, see SM [88]. It is therefore interesting to consider if true and false PMMs can be distinguished without having to construct a long uniform chain. Finally, throughout we assumed uniform parameters in the long chain limit, however, it is important to emphasise that this is a theoretical tool to determine the nature of PMMs. In realistic experimental chains there is no reason to assume uniform parameters. For instance, although gates can easily tune chemical potential, it is not expected that other parameters such as g -factor, SOI strength and direction, onsite U , and many more can be uniform, this could cause problems with the identification of MBSs in the longer chains [33, 90, 91].

Acknowledgments. This work was supported by the Swiss National Science Foundation and NCCR SPIN (Grant No. 51NF40-180604). This project received funding from the European Union’s Horizon 2020 research and innovation program (ERC Starting Grant, Grant Agreement No. 757725). H.F.L acknowledges support by the Georg H. Endress Foundation.

* henry.legg@unibas.ch

- [1] A Yu Kitaev, “Unpaired Majorana fermions in quantum wires,” *Physics-uspekhi* **44**, 131 (2001).
- [2] D. A. Ivanov, “Non-Abelian Statistics of Half-Quantum Vortices in p -Wave Superconductors,” *Phys. Rev. Lett.* **86**, 268–271 (2001).
- [3] A. Yu. Kitaev, “Fault-tolerant quantum computation by anyons,” *Annals of Physics* **303**, 2–30 (2003).
- [4] Chetan Nayak, Steven H. Simon, Ady Stern, Michael Freedman, and Sankar Das Sarma, “Non-Abelian anyons and topological quantum computation,” *Rev. Mod. Phys.* **80**, 1083–1159 (2008).
- [5] Steven R. Elliott and Marcel Franz, “Colloquium: Majorana fermions in nuclear, particle, and solid-state physics,” *Rev. Mod. Phys.* **87**, 137–163 (2015).
- [6] Roman M. Lutchyn, Jay D. Sau, and S. Das Sarma, “Majorana Fermions and a Topological Phase Transition in Semiconductor-Superconductor Heterostructures,” *Phys. Rev. Lett.* **105**, 077001 (2010).
- [7] Yuval Oreg, Gil Refael, and Felix von Oppen, “Helical Liquids and Majorana Bound States in Quantum Wires,” *Phys. Rev. Lett.* **105**, 177002 (2010).
- [8] Tudor D. Stanescu, Roman M. Lutchyn, and S. Das Sarma, “Majorana fermions in semiconductor nanowires,” *Phys. Rev. B* **84**, 144522 (2011).
- [9] V. Mourik, K. Zuo, S. M. Frolov, S. R. Plissard, E. P. A. M. Bakkers, and L. P. Kouwenhoven, “Signatures of Majorana Fermions in Hybrid Superconductor-Semiconductor Nanowire Devices,” *Science* **336**, 1003–1007 (2012).
- [10] Anindya Das, Yuval Ronen, Yonatan Most, Yuval Oreg, Moty Heiblum, and Hadas Shtrikman, “Zero-bias peaks and splitting in an Al-InAs nanowire topological superconductor as a signature of Majorana fermions,” *Nature Physics* **8**, 887–895 (2012).
- [11] M. T. Deng, C. L. Yu, G. Y. Huang, M. Larsson, P. Caroff, and H. Q. Xu, “Anomalous Zero-Bias Conductance Peak in a Nb-InSb Nanowire-Nb Hybrid Device,” *Nano Letters* **12**, 6414–6419 (2012).
- [12] Katharina Laubscher and Jelena Klinovaja, “Majorana bound states in semiconducting nanostructures,” *Journal of Applied Physics* **130**, 081101 (2021).
- [13] G. Kells, D. Meidan, and P. W. Brouwer, “Near-zero-energy end states in topologically trivial spin-orbit coupled superconducting nanowires with a smooth confinement,” *Phys. Rev. B* **86**, 100503 (2012).
- [14] Eduardo J. H. Lee, Xiaocheng Jiang, Ramón Aguado, Georgios Katsaros, Charles M. Lieber, and Silvano De Franceschi, “Zero-Bias Anomaly in a Nanowire Quantum Dot Coupled to Superconductors,” *Phys. Rev. Lett.* **109**, 186802 (2012).
- [15] Diego Rainis, Luka Trifunovic, Jelena Klinovaja, and Daniel Loss, “Towards a realistic transport modeling in a superconducting nanowire with Majorana fermions,” *Phys. Rev. B* **87**, 024515 (2013).
- [16] Dibyendu Roy, Nilanjan Bondyopadhyaya, and Sumanta Tewari, “Topologically trivial zero-bias conductance peak in semiconductor Majorana wires from boundary effects,” *Phys. Rev. B* **88**, 020502 (2013).
- [17] Andrzej Ptok, Aksel Kobińska, and Tadeusz Domański, “Controlling the bound states in a quantum-dot hybrid nanowire,” *Phys. Rev. B* **96**, 195430 (2017).
- [18] Chun-Xiao Liu, Jay D. Sau, Tudor D. Stanescu, and S. Das Sarma, “Andreev bound states versus Majorana bound states in quantum dot-nanowire-superconductor hybrid structures: Trivial versus topological zero-bias conductance peaks,” *Phys. Rev. B* **96**, 075161 (2017).
- [19] Christopher Moore, Tudor D. Stanescu, and Sumanta Tewari, “Two-terminal charge tunneling: Disentangling Majorana zero modes from partially separated Andreev bound states in semiconductor-superconductor heterostructures,” *Phys. Rev. B* **97**, 165302 (2018).
- [20] Christopher Moore, Chuanchang Zeng, Tudor D. Stanescu, and Sumanta Tewari, “Quantized zero-bias conductance plateau in semiconductor-superconductor heterostructures without topological Majorana zero modes,” *Phys. Rev. B* **98**, 155314 (2018).
- [21] Christopher Reeg, Olesia Dmytruk, Denis Chevallier, Daniel Loss, and Jelena Klinovaja, “Zero-energy Andreev bound states from quantum dots in proximitized Rashba nanowires,” *Phys. Rev. B* **98**, 245407 (2018).
- [22] Adriaan Vuik, Bas Nijholt, Anton R. Akhmerov, and Michael Wimmer, “Reproducing topological properties with quasi-Majorana states,” *SciPost Phys.* **7**, 061 (2019).
- [23] Tudor D. Stanescu and Sumanta Tewari, “Robust low-energy Andreev bound states in semiconductor-superconductor structures: Importance of partial separation of component Majorana bound states,” *Phys. Rev. B* **100**, 155429 (2019).
- [24] Benjamin D. Woods, Jun Chen, Sergey M. Frolov, and Tudor D. Stanescu, “Zero-energy pinning of topologically trivial bound states in multiband semiconductor-superconductor nanowires,” *Phys. Rev. B* **100**, 125407 (2019).
- [25] J. Chen, B. D. Woods, P. Yu, M. Hocevar, D. Car, S. R. Plissard, E. P. A. M. Bakkers, T. D. Stanescu, and S. M. Frolov, “Ubiquitous Non-Majorana Zero-Bias Conductance Peaks in Nanowire Devices,” *Phys. Rev. Lett.* **123**, 107703 (2019).
- [26] Oladunjoye A. Awoga, Jorge Cayao, and Annica M. Black-Schaffer, “Supercurrent Detection of Topologically Trivial Zero-Energy States in Nanowire Junctions,” *Phys. Rev. Lett.* **123**, 117001 (2019).
- [27] Elsa Prada, Pablo San-Jose, Michiel WA de Moor, Attila Geresdi, Eduardo JH Lee, Jelena Klinovaja, Daniel Loss, Jesper Nygård, Ramón Aguado, and Leo P Kouwenhoven, “From Andreev to Majorana bound states in hybrid superconductor-semiconductor nanowires,” *Nature Reviews Physics* **2**, 575–594 (2020).
- [28] Peng Yu, J Chen, M Gomanko, G Badawy, EPAM Bakkers, K Zuo, V Mourik, and SM Frolov, “Non-Majorana states yield nearly quantized conductance in proximatized nanowires,” *Nature Physics* **17**, 482–488 (2021).
- [29] Sankar Das Sarma and Haining Pan, “Disorder-induced zero-bias peaks in Majorana nanowires,” *Phys. Rev. B* **103**, 195158 (2021).
- [30] Marco Valentini, Fernando Peñaranda, Andrea Hofmann, Matthias Brauns, Robert Hauschild, Peter Krogstrup, Pablo San-Jose, Elsa Prada, Ramón Aguado, and Georgios Katsaros, “Nontopological zero-bias peaks in full-shell nanowires induced by flux-tunable Andreev states,” *Science* **373**, 82–88 (2021).
- [31] Richard Hess, Henry F. Legg, Daniel Loss, and Jelena

- Klinovaja, “Local and nonlocal quantum transport due to Andreev bound states in finite Rashba nanowires with superconducting and normal sections,” *Phys. Rev. B* **104**, 075405 (2021).
- [32] Richard Hess, Henry F. Legg, Daniel Loss, and Jelena Klinovaja, “Trivial Andreev Band Mimicking Topological Bulk Gap Reopening in the Nonlocal Conductance of Long Rashba Nanowires,” *Phys. Rev. Lett.* **130**, 207001 (2023).
- [33] Richard Hess, Henry F. Legg, Daniel Loss, and Jelena Klinovaja, “Prevalence of trivial zero-energy subgap states in nonuniform helical spin chains on the surface of superconductors,” *Phys. Rev. B* **106**, 104503 (2022).
- [34] Jay D Sau and S Das Sarma, “Realizing a robust practical Majorana chain in a quantum-dot-superconductor linear array,” *Nature communications* **3**, 964 (2012).
- [35] Martin Leijnse and Karsten Flensberg, “Parity qubits and poor man’s Majorana bound states in double quantum dots,” *Phys. Rev. B* **86**, 134528 (2012).
- [36] Ion C Fulga, Arbel Haim, Anton R Akhmerov, and Yuval Oreg, “Adaptive tuning of Majorana fermions in a quantum dot chain,” *New journal of physics* **15**, 045020 (2013).
- [37] Björn Sothmann, Jian Li, and Markus Büttiker, “Fractional Josephson effect in a quadruple quantum dot,” *New Journal of Physics* **15**, 085018 (2013).
- [38] Yantao Li, Arijit Kundu, Fan Zhong, and Babak Seradjeh, “Tunable Floquet Majorana fermions in driven coupled quantum dots,” *Phys. Rev. B* **90**, 121401 (2014).
- [39] Zhaoen Su, Alexandre B Tacla, Moira Hocoar, Diana Car, Sébastien R Plissard, Erik PAM Bakkers, Andrew J Daley, David Pekker, and Sergey M Frolov, “Andreev molecules in semiconductor nanowire double quantum dots,” *Nature communications* **8**, 585 (2017).
- [40] Athanasios Tsintzis, Rubén Seoane Souto, and Martin Leijnse, “Creating and detecting poor man’s Majorana bound states in interacting quantum dots,” *Phys. Rev. B* **106**, L201404 (2022).
- [41] Chun-Xiao Liu, Guanzhong Wang, Tom Dvir, and Michael Wimmer, “Tunable Superconducting Coupling of Quantum Dots via Andreev Bound States in Semiconductor-Superconductor Nanowires,” *Phys. Rev. Lett.* **129**, 267701 (2022).
- [42] Tom Dvir, Guanzhong Wang, Nick van Loo, Chun-Xiao Liu, Grzegorz P Mazur, Alberto Bordin, Sebastiaan LD Ten Haaf, Ji-Yin Wang, David van Driel, Francesco Zatelli, Xiang Li, Filip K. Malinowski, Sasa Gazibegovic, Ghada Badawy, Erik P. A. M. Bakkers, Michael Wimmer, and Leo P. Kouwenhoven, “Realization of a minimal Kitaev chain in coupled quantum dots,” *Nature* **614**, 445–450 (2023).
- [43] J. E. Sanches, L. T. Lustosa, L. S. Ricco, I. A. Shelykh, M. de Souza, M. S. Figueira, and A. C. Seridonio, “Fractionalization of Majorana-Ising-type quasiparticle excitations,” *Phys. Rev. B* **107**, 155144 (2023).
- [44] Chun-Xiao Liu, Haining Pan, F. Setiawan, Michael Wimmer, and Jay D. Sau, “Fusion protocol for Majorana modes in coupled quantum dots,” *Phys. Rev. B* **108**, 085437 (2023).
- [45] Rouven Koch, David van Driel, Alberto Bordin, Jose L. Lado, and Eliska Greplova, “Adversarial Hamiltonian learning of quantum dots in a minimal Kitaev chain,” *Phys. Rev. Appl.* **20**, 044081 (2023).
- [46] Rubén Seoane Souto, Athanasios Tsintzis, Martin Leijnse, and Jeroen Danon, “Probing Majorana localization in minimal Kitaev chains through a quantum dot,” *Phys. Rev. Res.* **5**, 043182 (2023).
- [47] Francesco Zatelli, David van Driel, Di Xu, Guanzhong Wang, Chun-Xiao Liu, Alberto Bordin, Bart Roovers, Grzegorz P. Mazur, Nick van Loo, Jan Cornelis Wolff, A. Mert Bozkurt, Ghada Badawy, Sasa Gazibegovic, Erik P. A. M. Bakkers, Michael Wimmer, Leo P. Kouwenhoven, and Tom Dvir, “Robust poor man’s Majorana zero modes using Yu-Shiba-Rusinov states,” (2023), arXiv:2311.03193 [cond-mat.mes-hall].
- [48] William Samuelson, Viktor Svensson, and Martin Leijnse, “Minimal quantum dot based Kitaev chain with only local superconducting proximity effect,” *Phys. Rev. B* **109**, 035415 (2024).
- [49] Athanasios Tsintzis, Rubén Seoane Souto, Karsten Flensberg, Jeroen Danon, and Martin Leijnse, “Majorana Qubits and Non-Abelian Physics in Quantum Dot-Based Minimal Kitaev Chains,” *PRX Quantum* **5**, 010323 (2024).
- [50] D. Michel Pino, Rubén Seoane Souto, and Ramón Aguado, “Minimal Kitaev-transmon qubit based on double quantum dots,” *Phys. Rev. B* **109**, 075101 (2024).
- [51] Juan Daniel Torres Luna, A. Mert Bozkurt, Michael Wimmer, and Chun-Xiao Liu, “Flux-tunable Kitaev chain in a quantum dot array,” (2024), arXiv:2402.07575 [cond-mat.mes-hall].
- [52] Alberto Bordin, Chun-Xiao Liu, Tom Dvir, Francesco Zatelli, Sebastiaan L. D. ten Haaf, David van Driel, Guanzhong Wang, Nick van Loo, Thomas van Caekenberghe, Jan Cornelis Wolff, Yining Zhang, Ghada Badawy, Sasa Gazibegovic, Erik P. A. M. Bakkers, Michael Wimmer, Leo P. Kouwenhoven, and Grzegorz P. Mazur, “Signatures of Majorana protection in a three-site Kitaev chain,” (2024), arXiv:2402.19382 [cond-mat.suprcon].
- [53] Péter Boross and András Pályi, “Braiding-based quantum control of a Majorana qubit built from quantum dots,” *Phys. Rev. B* **109**, 125410 (2024).
- [54] Zhi-Hai Liu, Chuanchang Zeng, and H. Q. Xu, “Coupling of quantum-dot states via elastic-cotunneling and crossed Andreev reflection in a minimal Kitaev chain,” (2024), arXiv:2403.08636 [cond-mat.mes-hall].
- [55] Kostas Vilkelis, Antonio Manesco, Juan Daniel Torres Luna, Sebastian Miles, Michael Wimmer, and Anton Akhmerov, “Fermionic quantum computation with Cooper pair splitters,” *SciPost Phys.* **16**, 135 (2024).
- [56] A. Mert Bozkurt, Sebastian Miles, Sebastiaan L. D. ten Haaf, Chun-Xiao Liu, Fabian Hassler, and Michael Wimmer, “Interaction-induced strong zero modes in short quantum dot chains with time-reversal symmetry,” (2024), arXiv:2405.14940 [cond-mat.mes-hall].
- [57] David van Driel, Rouven Koch, Vincent P. M. Sietes, Sebastiaan L. D. ten Haaf, Chun-Xiao Liu, Francesco Zatelli, Bart Roovers, Alberto Bordin, Nick van Loo, Guanzhong Wang, Jan Cornelis Wolff, Grzegorz P. Mazur, Tom Dvir, Ivan Kulesh, Qingzhen Wang, A. Mert Bozkurt, Sasa Gazibegovic, Ghada Badawy, Erik P. A. M. Bakkers, Michael Wimmer, Srijit Goswami, Jose L. Lado, Leo P. Kouwenhoven, and Eliska Greplova, “Cross-Platform Autonomous Control of Minimal Kitaev Chains,” (2024), arXiv:2405.04596 [cond-mat.mes-hall].
- [58] D. Michel Pino, Yigal Meir, and Ramón Aguado, “Thermodynamics of Non-Hermitian Josephson junctions with

- exceptional points,” (2024), arXiv:2405.02387 [cond-mat.mes-hall].
- [59] Max Geier, Rubén Seoane Souto, Jens Schulenburg, Swana Asaad, Martin Leijnse, and Karsten Flensberg, “Fermion-parity qubit in a proximitized double quantum dot,” *Phys. Rev. Res.* **6**, 023281 (2024).
- [60] Sebastiaan LD Ten Haaf, Qingzhen Wang, A Mert Bozkurt, Chun-Xiao Liu, Ivan Kulesh, Philip Kim, Di Xiao, Candice Thomas, Michael J Manfra, Tom Dvir, Michael Wimmer, and Srijit Goswami, “A two-site Kitaev chain in a two-dimensional electron gas,” *Nature* **630**, 329–334 (2024).
- [61] Mátyás Kocsis, Zoltán Scherübl, Gergő Fülöp, Péter Makk, and Szabolcs Csonka, “Strong nonlocal tuning of the current-phase relation of a quantum dot based Andreev molecule,” *Phys. Rev. B* **109**, 245133 (2024).
- [62] Jorge Cayao, “Emergent pair symmetries in systems with poor man’s Majorana modes,” (2024), arXiv:2406.17508 [cond-mat.mes-hall].
- [63] Sebastian Miles, David van Driel, Michael Wimmer, and Chun-Xiao Liu, “Kitaev chain in an alternating quantum dot-Andreev bound state array,” *Phys. Rev. B* **110**, 024520 (2024).
- [64] Jorge Cayao and Ramón Aguado, “Non-Hermitian minimal Kitaev chains,” (2024), arXiv:2406.18974 [cond-mat.mes-hall].
- [65] Chun-Xiao Liu, Sebastian Miles, Alberto Bordin, Sebastiaan L. D. ten Haaf, A. Mert Bozkurt, and Michael Wimmer, “Protocol for scaling up a sign-ordered Kitaev chain without magnetic flux control,” (2024), arXiv:2407.04630 [cond-mat.mes-hall].
- [66] Miguel Alvarado, Alfredo Levy Yeyati, Ramón Aguado, and Rubén Seoane Souto, “Interplay between Majorana and Shiba states in a minimal Kitaev chain coupled to a superconductor,” (2024), arXiv:2407.07050 [cond-mat.mes-hall].
- [67] Viktor Svensson and Martin Leijnse, “Quantum-dot-based Kitaev chains: Majorana quality measures and scaling with increasing chain length,” (2024), arXiv:2407.09211 [cond-mat.mes-hall].
- [68] Álvaro Gómez-León, Marco Schirò, and Olesia Dmytruk, “High-quality poor man’s Majorana bound states from cavity embedding,” (2024), arXiv:2407.12088 [cond-mat.mes-hall].
- [69] Haining Pan, Sankar Das Sarma, and Chun-Xiao Liu, “Rabi and Ramsey oscillations of a Majorana qubit in a quantum dot-superconductor array,” (2024), arXiv:2407.16750 [cond-mat.mes-hall].
- [70] Bradraj Pandey and Elbio Dagotto, “Dynamics and Fusion of Majorana Zero Modes in Quantum-dot based Interacting Kitaev Chains,” (2024), arXiv:2407.20783 [cond-mat.supr-con].
- [71] Chun-Xiao Liu, A Mert Bozkurt, Francesco Zatelli, Sebastiaan LD ten Haaf, Tom Dvir, and Michael Wimmer, “Enhancing the excitation gap of a quantum-dot-based Kitaev chain,” *Communications Physics* **7**, 235 (2024).
- [72] Jacob Benestad, Athanasios Tsintzis, Rubén Seoane Souto, Martin Leijnse, Evert van Nieuwenburg, and Jeroen Danon, “Machine-learned tuning of artificial Kitaev chains from tunneling spectroscopy measurements,” *Phys. Rev. B* **110**, 075402 (2024).
- [73] Melina Luethi, Henry F. Legg, Daniel Loss, and Jelena Klinovaja, “From perfect to imperfect poor man’s Majoranas in minimal Kitaev chains,” (2024), arXiv:2408.03071 [cond-mat.mes-hall].
- [74] Patrik Recher, Eugene V. Sukhorukov, and Daniel Loss, “Andreev tunneling, Coulomb blockade, and resonant transport of nonlocal spin-entangled electrons,” *Phys. Rev. B* **63**, 165314 (2001).
- [75] Gordey B Lesovik, Thierry Martin, and Gianni Blatter, “Electronic entanglement in the vicinity of a superconductor,” *The European Physical Journal B-Condensed Matter and Complex Systems* **24**, 287–290 (2001).
- [76] G. Falci, D. Feinberg, and F. W. J. Hekking, “Correlated tunneling into a superconductor in a multiprobe hybrid structure,” *Europhysics Letters* **54**, 255 (2001).
- [77] V Bouchiat, N Chtchelkatchev, D Feinberg, G B Lesovik, T Martin, and J Torrès, “Single-walled carbon nanotube-superconductor entangler: noise correlations and Einstein-Podolsky-Rosen states,” *Nanotechnology* **14**, 77 (2002).
- [78] D Feinberg, “Andreev scattering and cotunneling between two superconductor-normal metal interfaces: the dirty limit,” *The European Physical Journal B-Condensed Matter and Complex Systems* **36**, 419–422 (2003).
- [79] Lukas Hofstetter, Sa Csonka, Jesper Nygård, and C Schönenberger, “Cooper pair splitter realized in a two-quantum-dot Y-junction,” *Nature* **461**, 960–963 (2009).
- [80] L. G. Herrmann, F. Portier, P. Roche, A. Levy Yeyati, T. Kontos, and C. Strunk, “Carbon Nanotubes as Cooper-Pair Beam Splitters,” *Phys. Rev. Lett.* **104**, 026801 (2010).
- [81] Guanzhong Wang, Tom Dvir, Grzegorz P Mazur, Chun-Xiao Liu, Nick van Loo, Sebastiaan LD Ten Haaf, Alberto Bordin, Sasa Gazibegovic, Ghada Badawy, Erik PAM Bakkers, Michael Wimmer, and Kouwenhoven Leo P, “Singlet and triplet Cooper pair splitting in hybrid superconducting nanowires,” *Nature* **612**, 448–453 (2022).
- [82] Olivér Kürtösy, Zoltán Scherübl, Gergő Fülöp, István Endre Lukács, Thomas Kanne, Jesper Nygård, Péter Makk, and Szabolcs Csonka, “Parallel InAs nanowires for Cooper pair splitters with Coulomb repulsion,” *npj Quantum Materials* **7**, 88 (2022).
- [83] Damaz de Jong, Christian G. Prosko, Lin Han, Filip K. Malinowski, Yu Liu, Leo P. Kouwenhoven, and Wolfgang Pfaff, “Controllable Single Cooper Pair Splitting in Hybrid Quantum Dot Systems,” *Phys. Rev. Lett.* **131**, 157001 (2023).
- [84] Alberto Bordin, Guanzhong Wang, Chun-Xiao Liu, Sebastiaan L. D. ten Haaf, Nick van Loo, Grzegorz P. Mazur, Di Xu, David van Driel, Francesco Zatelli, Sasa Gazibegovic, Ghada Badawy, Erik P. A. M. Bakkers, Michael Wimmer, Leo P. Kouwenhoven, and Tom Dvir, “Tunable Crossed Andreev Reflection and Elastic Cotunneling in Hybrid Nanowires,” *Phys. Rev. X* **13**, 031031 (2023).
- [85] Qingzhen Wang, Sebastiaan LD Ten Haaf, Ivan Kulesh, Di Xiao, Candice Thomas, Michael J Manfra, and Srijit Goswami, “Triplet correlations in Cooper pair splitters realized in a two-dimensional electron gas,” *Nature Communications* **14**, 4876 (2023).
- [86] Alberto Bordin, Xiang Li, David van Driel, Jan Cornelis Wolff, Qingzhen Wang, Sebastiaan L. D. ten Haaf, Guanzhong Wang, Nick van Loo, Leo P. Kouwenhoven, and Tom Dvir, “Crossed Andreev Reflection and Elastic

- Cotunneling in Three Quantum Dots Coupled by Superconductors,” *Phys. Rev. Lett.* **132**, 056602 (2024).
- [87] Marco Valentini, Rubén Seoane Souto, Maksim Borovkov, Peter Krogstrup, Yigal Meir, Martin Leijnse, Jeroen Danon, and Georgios Katsaros, “Subgap-state-mediated transport in superconductor–semiconductor hybrid islands: Weak and strong coupling regimes,” (2024), arXiv:2407.05195 [cond-mat.mes-hall].
- [88] Supplemental Material.
- [89] Christoph W Groth, Michael Wimmer, Anton R Akhmerov, and Xavier Waintal, “Kwant: a software package for quantum transport,” *New Journal of Physics* **16**, 063065 (2014).
- [90] Richard Hess, Henry F. Legg, Daniel Loss, and Jelena Klinovaja, “Trivial Andreev Band Mimicking Topological Bulk Gap Reopening in the Nonlocal Conductance of Long Rashba Nanowires,” *Phys. Rev. Lett.* **130**, 207001 (2023).
- [91] Henry F. Legg, Richard Hess, Daniel Loss, and Jelena Klinovaja, “Reply to Antipov et al., *Microsoft Quantum*: ”Comment on Hess et al. *Phys. Rev. Lett.* 130, 207001 (2023)”,” (2024), arXiv:2308.10669 [cond-mat.mes-hall].

Supplementary material for: The fate of poor man's Majoranas in the long Kitaev chain limit

Melina Luethi^{†,1}, Henry F. Legg^{†,1}, Daniel Loss,¹ and Jelena Klinovaja¹

¹*Department of Physics, University of Basel, Klingelbergstrasse 82, CH-4056 Basel, Switzerland*

[†]*These authors contributed equally to this work.*

(Dated: August 20, 2024)

I. HAMILTONIANS USED FOR THE CALCULATIONS

In this section, we present all Hamiltonians used for this work. They are all based on Eq. (1) of the main text.

A. Second quantized form of the Hamiltonian

Since the total electron parity is conserved by the Hamiltonian given in Eq. (1), we consider the total even and total odd parity sector separately. For the even parity sector, the basis is

$$\begin{aligned} \Psi_{\text{even}} = & (|0, 0, 0\rangle, |\uparrow\downarrow, 0, 0\rangle, |\uparrow, \uparrow, 0\rangle, |\downarrow, \uparrow, 0\rangle, |\uparrow, \downarrow, 0\rangle, \\ & |\downarrow, \downarrow, 0\rangle, |0, \uparrow\downarrow, 0\rangle, |\uparrow\downarrow, \uparrow\downarrow, 0\rangle, |\uparrow, 0, \uparrow\rangle, |\downarrow, 0, \uparrow\rangle, |0, \uparrow, \uparrow\rangle, \\ & |\uparrow\downarrow, \uparrow, \uparrow\rangle, |0, \downarrow, \uparrow\rangle, |\uparrow\downarrow, \downarrow, \uparrow\rangle, |\uparrow, \uparrow\downarrow, \uparrow\rangle, |\downarrow, \uparrow\downarrow, \uparrow\rangle, |\uparrow, 0, \downarrow\rangle, \\ & |\downarrow, 0, \downarrow\rangle, |0, \uparrow, \downarrow\rangle, |\uparrow\downarrow, \uparrow, \downarrow\rangle, |0, \downarrow, \downarrow\rangle, |\uparrow\downarrow, \downarrow, \downarrow\rangle, |\uparrow, \uparrow\downarrow, \downarrow\rangle, \\ & |\downarrow, \uparrow\downarrow, \downarrow\rangle, |0, 0, \uparrow\downarrow\rangle, |\uparrow\downarrow, 0, \uparrow\downarrow\rangle, |\uparrow, \uparrow, \uparrow\downarrow\rangle, |\downarrow, \uparrow, \uparrow\downarrow\rangle, \\ & |\uparrow, \downarrow, \uparrow\downarrow\rangle, |\downarrow, \downarrow, \uparrow\downarrow\rangle, |0, \uparrow\downarrow, \uparrow\downarrow\rangle, |\uparrow\downarrow, \uparrow\downarrow, \uparrow\downarrow\rangle) \end{aligned} \quad (1)$$

and for the odd parity sector, the basis is

$$\begin{aligned} \Psi_{\text{odd}} = & (|\uparrow, 0, 0\rangle, |\downarrow, 0, 0\rangle, |0, \uparrow, 0\rangle, |\uparrow\downarrow, \uparrow, 0\rangle, |0, \downarrow, 0\rangle, \\ & |\uparrow\downarrow, \downarrow, 0\rangle, |\uparrow, \uparrow\downarrow, 0\rangle, |\downarrow, \uparrow\downarrow, 0\rangle, |0, 0, \uparrow\rangle, |\uparrow\downarrow, 0, \uparrow\rangle, |\uparrow, \uparrow, \uparrow\rangle, \\ & |\downarrow, \uparrow, \uparrow\rangle, |\uparrow, \downarrow, \uparrow\rangle, |\downarrow, \downarrow, \uparrow\rangle, |0, \uparrow\downarrow, \uparrow\rangle, |\uparrow\downarrow, \uparrow\downarrow, \uparrow\rangle, |0, 0, \downarrow\rangle, \\ & |\uparrow\downarrow, 0, \downarrow\rangle, |\uparrow, \uparrow, \downarrow\rangle, |\downarrow, \uparrow, \downarrow\rangle, |\uparrow, \downarrow, \downarrow\rangle, |\downarrow, \downarrow, \downarrow\rangle, |0, \uparrow\downarrow, \downarrow\rangle, \\ & |\uparrow\downarrow, \uparrow\downarrow, \downarrow\rangle, |\uparrow, 0, \uparrow\downarrow\rangle, |\downarrow, 0, \uparrow\downarrow\rangle, |0, \uparrow, \uparrow\downarrow\rangle, |\uparrow\downarrow, \uparrow, \uparrow\downarrow\rangle, \\ & |0, \downarrow, \uparrow\downarrow\rangle, |\uparrow\downarrow, \downarrow, \uparrow\downarrow\rangle, |\uparrow, \uparrow\downarrow, \uparrow\downarrow\rangle, |\downarrow, \uparrow\downarrow, \uparrow\downarrow\rangle). \end{aligned} \quad (2)$$

In total, there are $4^3 = 64$ states, thus 32 states per parity sector. The corresponding Hamiltonians $\mathcal{H}_{\text{even}}$ and \mathcal{H}_{odd} are thus 32×32 matrices and we do not give their explicit form here. However, their matrix elements $(\mathcal{H}_{\text{even/odd}})_{ij}$ are calculated as follows

$$(\mathcal{H}_{\text{even}})_{ij} = \langle \Psi_{\text{even},i} | H | \Psi_{\text{even},j} \rangle \quad (3a)$$

$$(\mathcal{H}_{\text{odd}})_{ij} = \langle \Psi_{\text{odd},i} | H | \Psi_{\text{odd},j} \rangle, \quad (3b)$$

where H is the Hamiltonian defined in Eq. (1) of the main text and $\Psi_{\text{even},i}$ ($\Psi_{\text{odd},i}$) is the i -th element of the even (odd) basis defined in Eq. (1) [Eq. (2)] of the SM. The eigenvectors of the matrices defined in Eq. (3) are labeled as $|\Psi_a^{\text{even}}\rangle$ and $|\Psi_a^{\text{odd}}\rangle$, respectively, and the corresponding eigenvalues are E_a^{even} and E_a^{odd} , where a numbers the

eigenstates and eigenvalues. For short chains, the eigenvectors and eigenvalues are calculated using exact diagonalization. For the long chain limit, the approach of the density matrix renormalization group (DMRG) [1–3] is used. The eigenvectors and eigenvalues are used to calculate ΔE [defined in Eq. (3) in the main text], $\Delta Q_{L/R}$ [defined in Eq. (4) in the main text], $M_{L/R}$ [defined in Eq. (5) in the main text], and E_{ex} [defined in Eq. (6) in the main text].

B. BdG Hamiltonian

If $U = 0$, one can work with the BdG form of the Hamiltonian given in Eq. (1). This form can also be trivially extended to the long chain limit with M sites [M must be odd, $(M+1)/2$ of these sites are normal, $(M-1)/2$ are superconducting sites]. Introducing the Nambu basis

$$\Psi_j = (c_{j,\uparrow}, c_{j,\downarrow}, c_{j,\uparrow}^\dagger, c_{j,\downarrow}^\dagger) \quad (4)$$

the Hamiltonian is given by

$$\begin{aligned} H_{\text{BdG}} = & \frac{1}{2} \sum_{j=1}^M \Psi_j^\dagger [(\mu_j + \Delta_{Z,j} \sigma_z) \tau_z + \Delta_j \sigma_y \tau_y] \Psi_j \\ & + t \sum_{j=1}^{M-1} \Psi_{j+1}^\dagger \left[\cos\left(\frac{\Phi_{\text{SOI}}}{2}\right) + i \sin\left(\frac{\Phi_{\text{SOI}}}{2}\right) \sigma_y \right] \tau_z \Psi_j \\ & + \text{H.c.}, \end{aligned} \quad (5)$$

where the chemical potential, Zeeman energy, and superconducting gap are position-dependent as follows

$$\mu_j = \begin{cases} \mu & \text{if } j \bmod 2 = 1 \\ \mu_M & \text{if } j \bmod 2 = 0 \end{cases} \quad (6)$$

$$\Delta_{Z,j} = \begin{cases} \Delta_Z & \text{if } j \bmod 2 = 1 \\ 0 & \text{if } j \bmod 2 = 0 \end{cases} \quad (7)$$

$$\Delta_j = \begin{cases} 0 & \text{if } j \bmod 2 = 1 \\ \Delta & \text{if } j \bmod 2 = 0 \end{cases}, \quad (8)$$

where μ , μ_M , Δ_Z , and Δ are as defined in the main text. When $U = 0$ the BdG Hamiltonian is used to calculate the long chain limit [shown, e.g., in Fig. 3 of the main text], topological invariants (see Sec. III of the SM), and all conductance data [shown, e.g., in Figs. 4 and 5 of the main text].

II. ANALYTICS OF THE TRIVIAL STATES IN THE ROT

In this section, we explain the trivial fourfold degenerate zero-energy state at $\Delta_Z/\Delta = 0.8$ in Fig. 3(f) in the main text. Although many of the false PMMs are related to such a fourfold degenerate zero-energy state, we emphasize that this is not necessary for false PMMs.

Let us consider a double QD system without superconductivity and where only one of the QDs has a Zeeman term. Using the basis $\Psi = (d_{1,\uparrow}, d_{1,\downarrow}, d_{2,\uparrow}, d_{2,\downarrow})^T$, the double-QD system is described by the Hamiltonian

$$H_{2\text{QD}} = \Psi^\dagger \mathcal{H}_{2\text{QD}} \Psi, \quad \text{where} \quad (9a)$$

$$\mathcal{H}_{2\text{QD}} = \begin{pmatrix} \mu + \Delta_Z & 0 & t \cos\left(\frac{\Phi_{\text{SOI}}}{2}\right) & t \sin\left(\frac{\Phi_{\text{SOI}}}{2}\right) \\ 0 & \mu - \Delta_Z & -t \sin\left(\frac{\Phi_{\text{SOI}}}{2}\right) & t \cos\left(\frac{\Phi_{\text{SOI}}}{2}\right) \\ t \cos\left(\frac{\Phi_{\text{SOI}}}{2}\right) & -t \sin\left(\frac{\Phi_{\text{SOI}}}{2}\right) & \mu_M & 0 \\ t \sin\left(\frac{\Phi_{\text{SOI}}}{2}\right) & t \cos\left(\frac{\Phi_{\text{SOI}}}{2}\right) & 0 & \mu_M \end{pmatrix}. \quad (9b)$$

Using $\mu/\Delta = 0.593$, $\mu_M/\Delta = -3.836$, $t/\Delta = 0.99$, and $\Phi_{\text{SOI}} = 0.44\pi$, the parameters for Fig. 3(f) of the main text, we find that $H_{2\text{QD}}$ has a zero-energy state at $\Delta_Z/\Delta = 0.849$. The corresponding eigenstate is

$$\Psi = (0, 0.968, -0.159, 0.193)^T, \quad (10)$$

which is mostly localized on the first QD. As a result of this, adding a superconducting pairing potential to the second dot does not significantly change the solution, except that it becomes doubly degenerate due to particle-hole symmetry. Additionally, adding more QDs to the right of the second QD has little effect on this highly localized zero-energy state. Therefore, this explains the appearance of a highly localized zero-energy state on the left end of the long chain. One can argue equivalently for the right end of the long chain, and therefore the degeneracy doubles, leading to a four-fold degenerate, highly localized zero-energy state in a long chain. In Fig. 3(f) of the main text, we find the fourfold degenerate zero-energy state at $\Delta_Z/\Delta \approx 0.8$, not at $\Delta_Z/\Delta = 0.849$. We explain this difference by the fact that the eigenstate is not perfectly localized to only the first QD, which means that adding superconductivity and more QDs affects the state slightly.

III. TOPOLOGICAL INVARIANT

To calculate the topological invariant, one needs to consider an infinitely long chain. This is possible only for the case $U = 0$. The unit cell consist of a normal QD (a white dot in Fig. 1(b) of the main text) and a superconducting QD (a gray dot in Fig. 1(b) of the main text). The basis is thus given by

$$\Psi_k = \left(d_{\uparrow,k}, d_{\downarrow,k}, d_{\uparrow,-k}^\dagger, d_{\downarrow,-k}^\dagger, c_{\uparrow,k}, c_{\downarrow,k}, c_{\uparrow,-k}^\dagger, c_{\downarrow,-k}^\dagger \right)^T, \quad (11)$$

where $d_{\sigma,k}^\dagger$ ($c_{\sigma,k}^\dagger$) creates a particle of spin σ and momentum k on the normal (superconducting) QD. The infinite chain Hamiltonian in momentum space is given by

$$H_{\text{inf}}(k) = \Psi_k^\dagger \mathcal{H}_{\text{inf}}(k) \Psi_k \quad (12a)$$

$$\begin{aligned} \mathcal{H}_{\text{inf}}(k) = & (\mu + \Delta_Z \sigma_z) \tau_z \frac{\eta_0 + \eta_z}{2} + \mu_M \tau_z \frac{\eta_0 - \eta_z}{2} \\ & + t \cos(\Phi_{\text{SOI}}) \tau_z \{ \eta_x [1 + \cos(ka)] + \eta_y \sin(ka) \} \\ & - t \sin(\Phi_{\text{SOI}}) \sigma_y \tau_z \{ \eta_x \sin(ka) + \eta_y [1 - \cos(ka)] \} \\ & - \Delta \sigma_y \tau_y \frac{\eta_0 - \eta_z}{2}, \end{aligned} \quad (12b)$$

where σ_α are the Pauli matrices acting in spin space, τ_α the Pauli matrices acting in particle-hole space, η_α the Pauli matrices acting in the first QD-second QD space, k is the momentum, and a is the unit cell spacing. The topological invariant Q_{Z_2} is then given by [4]

$$Q_{Z_2} = \text{sign} \{ \text{Pf} [H_{\text{inf}}(ka = 0)] \text{Pf} [H_{\text{inf}}(ka = \pi)] \}. \quad (13)$$

If $Q_{Z_2} = 1$, the system is trivial and if $Q_{Z_2} = -1$, the system is topological.

IV. FURTHER EXAMPLES OF TRUE AND FALSE PMMS

In the main text, we have given just one example of a false PMM, i.e., a near-zero-energy state that is highly localized but that is not related to a topological MBS in the long chain limit, and one example of a true PMM, i.e., a near-zero-energy state that is highly localized and that is related to a topological MBS in the long chain limit. In this section, we give additional examples of a true and several false PMMs. We note that we present mainly false PMMs here and leave the discussion of the prevalence of true versus false PMMs for future work.

A. Energy difference, charge difference, and Majorana polarization

In Figs. 1-11 of the SM, we present the energy difference ΔE [defined in Eq. (3) in the main text, panels (a) and (d)], the charge difference ΔQ_j [defined in Eq. (4) in the main text, panels (b) and (e)], the Majorana polarization [defined in Eq. (5) in the main text, panels (c) and (f)], and the excitation gap E_{ex} [defined in Eq. (6) in the main text] for true and false PMMs. All calculations are done in the second quantized formulation of the Hamiltonian given in Eq. (1) of the main text. The black circled areas correspond to the ROT, which is defined in Eq. (7) of the main text. We show both examples where the on-site Coulomb repulsion is zero, i.e., $U = 0$, and examples where $U > 0$. Values for t and Φ_{SOI} were set using random values chosen from a uniform distribution in the t - Φ_{SOI} parameter space. Likewise, for the examples with $U > 0$, values for U were set using random values from a uniform distribution.

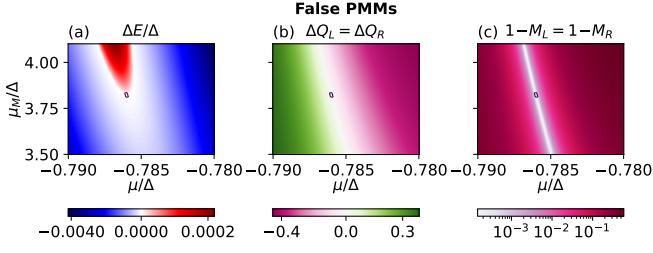


FIG. 1. The parameters are $t/\Delta = 0.24$, $\Phi_{\text{SOI}} = 0.42\pi$, $U = 0$, and $\Delta_Z/\Delta = 0.8$. The threshold values for the ROT are $\Delta E_{\text{th}}/\Delta = 10^{-5}$, $\Delta Q_{\text{th}} = 0.01$, $M_{\text{th}} = 0.01$, and the maximum excitation gap in the ROT is $E_{\text{ex}}/\Delta = 0.007$.

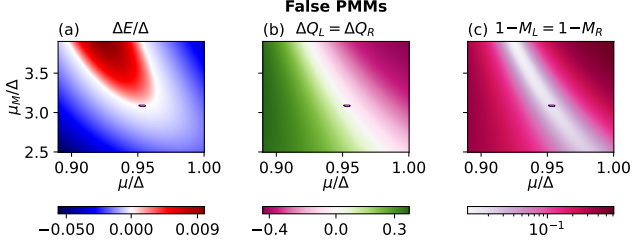


FIG. 2. The parameters are $t/\Delta = 0.7$, $\Phi_{\text{SOI}} = 0.38\pi$, $U = 0$, and $\Delta_Z/\Delta = 0.8$. The threshold values for the ROT are $\Delta E_{\text{th}}/\Delta = 10^{-4}$, $\Delta Q_{\text{th}} = 0.02$, $M_{\text{th}} = 0.02$, and the maximum excitation gap in the ROT is $E_{\text{ex}}/\Delta = 0.097$.

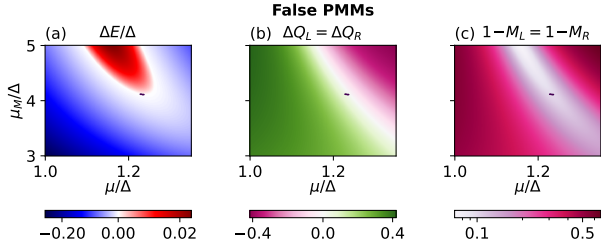


FIG. 3. The parameters are $t/\Delta = 1.27$, $\Phi_{\text{SOI}} = 0.38\pi$, $U = 0$, and $\Delta_Z/\Delta = 0.8$. The threshold values for the ROT are $\Delta E_{\text{th}}/\Delta = 10^{-4}$, $\Delta Q_{\text{th}} = 0.1$, $M_{\text{th}} = 0.1$, and the maximum excitation gap in the ROT is $E_{\text{ex}}/\Delta = 0.218$.

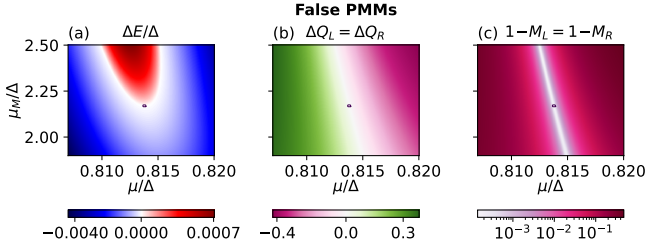


FIG. 4. The parameters are $t/\Delta = 0.19$, $\Phi_{\text{SOI}} = 0.36\pi$, $U = 0$, and $\Delta_Z/\Delta = 0.8$. The threshold values for the ROT are $\Delta E_{\text{th}}/\Delta = 10^{-5}$, $\Delta Q_{\text{th}} = 0.01$, $M_{\text{th}} = 0.01$, and the maximum excitation gap in the ROT is $E_{\text{ex}}/\Delta = 0.012$.

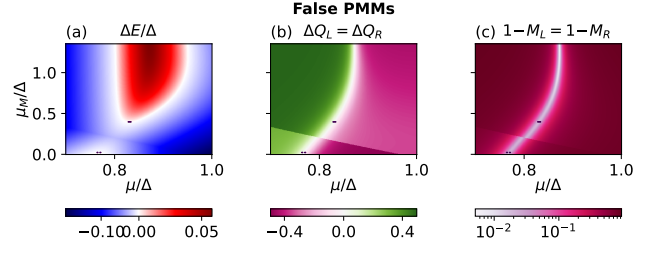


FIG. 5. The parameters are $t/\Delta = 0.41$, $\Phi_{\text{SOI}} = 0.06\pi$, $U = 0$, and $\Delta_Z/\Delta = 0.8$. The threshold values for the ROT are $\Delta E_{\text{th}}/\Delta = 10^{-4}$, $\Delta Q_{\text{th}} = 0.05$, $M_{\text{th}} = 0.05$, and the maximum excitation gap in the ROT is $E_{\text{ex}}/\Delta = 0.056$.

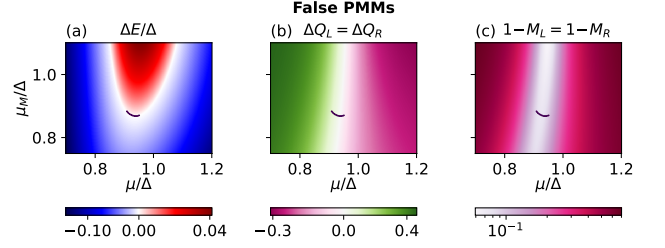


FIG. 6. The parameters are $t/\Delta = 0.64$, $\Phi_{\text{SOI}} = 0.12\pi$, $U = 0$, and $\Delta_Z/\Delta = 0.8$. The threshold values for the ROT are $\Delta E_{\text{th}}/\Delta = 10^{-4}$, $\Delta Q_{\text{th}} = 0.1$, $M_{\text{th}} = 0.1$, and the maximum excitation gap in the ROT is $E_{\text{ex}}/\Delta = 0.195$.

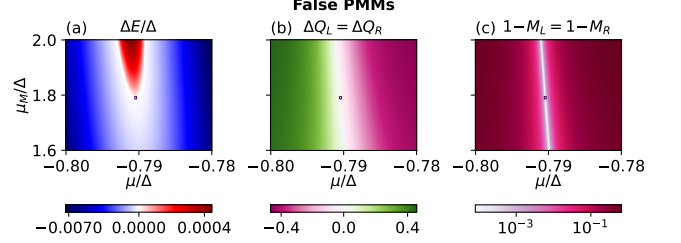


FIG. 7. The parameters are $t/\Delta = 0.15$, $\Phi_{\text{SOI}} = 0.34\pi$, $U = 0$, and $\Delta_Z/\Delta = 0.8$. The threshold values for the ROT are $\Delta E_{\text{th}}/\Delta = 10^{-5}$, $\Delta Q_{\text{th}} = 0.01$, $M_{\text{th}} = 0.01$, and the maximum excitation gap in the ROT is $E_{\text{ex}}/\Delta = 0.009$.

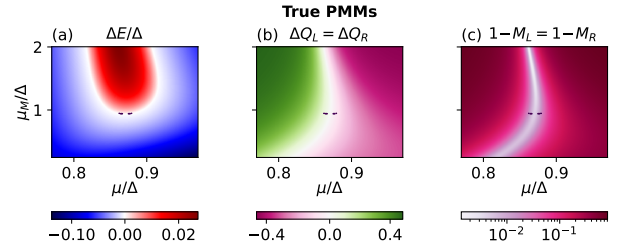


FIG. 8. The parameters are $t/\Delta = 0.4$, $\Phi_{\text{SOI}} = 0.22\pi$, $U/\Delta = 4.69$, and $\Delta_Z/\Delta = 0.8$. The threshold values for the ROT are $\Delta E_{\text{th}}/\Delta = 10^{-4}$, $\Delta Q_{\text{th}} = 0.07$, $M_{\text{th}} = 0.07$, and the maximum excitation gap in the ROT is $E_{\text{ex}}/\Delta = 0.107$.

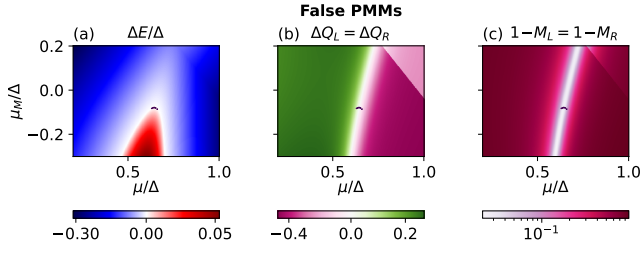


FIG. 9. The parameters are $t/\Delta = 0.6$, $\Phi_{\text{SOI}} = 0.06\pi$, $U/\Delta = 4.68$, and $\Delta_Z/\Delta = 0.8$. The threshold values for the ROT are $\Delta E_{\text{th}}/\Delta = 10^{-4}$, $\Delta Q_{\text{th}} = 0.1$, $M_{\text{th}} = 0.1$, and the maximum excitation gap in the ROT is $E_{\text{ex}}/\Delta = 0.103$.

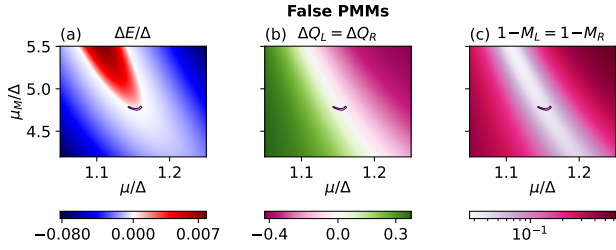


FIG. 10. The parameters are $t/\Delta = 1.29$, $\Phi_{\text{SOI}} = 0.46\pi$, $U/\Delta = 4.31$, and $\Delta_Z/\Delta = 0.8$. The threshold values for the ROT are $\Delta E_{\text{th}}/\Delta = 10^{-4}$, $\Delta Q_{\text{th}} = 0.05$, $M_{\text{th}} = 0.05$, and the maximum excitation gap in the ROT is $E_{\text{ex}}/\Delta = 0.070$.

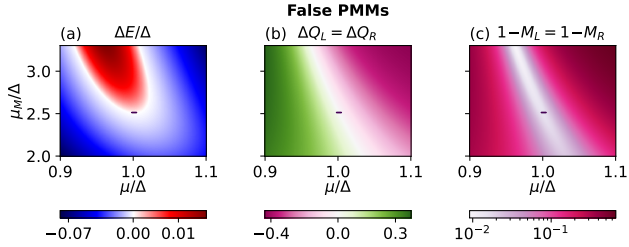


FIG. 11. The parameters are $t/\Delta = 0.76$, $\Phi_{\text{SOI}} = 0.38\pi$, $U = 3.81$, and $\Delta_Z/\Delta = 0.8$. The threshold values for the ROT are $\Delta E_{\text{th}}/\Delta = 10^{-4}$, $\Delta Q_{\text{th}} = 0.02$, $M_{\text{th}} = 0.02$, and the maximum excitation gap in the ROT is $E_{\text{ex}}/\Delta = 0.128$.

B. Energy spectrum vs. Zeeman energy

In Figs. 12-18, we present the energy spectrum (black dots) of the Hamiltonian as a function of the Zeeman energy Δ_Z in the long chain limit, and the topological invariant (magenta line) in the infinite chain limit (see also Sec. III). With this, we determine if a ROT is connected to topological MBSs or if it is connected to highly localized trivial states. The Zeeman energy value $\Delta_Z/\Delta = 0.8$ signifies the Zeeman energy at which we consider all ROT in Figs. 1-11. All calculations for $U = 0$ are done using the BdG formulation of the Hamiltonian given in Eq. (1) of the main text. For the datasets with finite U , we use DMRG [1–3], see Sec. IV B 1.

For the parameter sets with $U = 0$, we see that at $\Delta_Z/\Delta = 0.8$, none of the parameter sets presented in this section are related to topological MBSs, instead they all result in false PMMs.

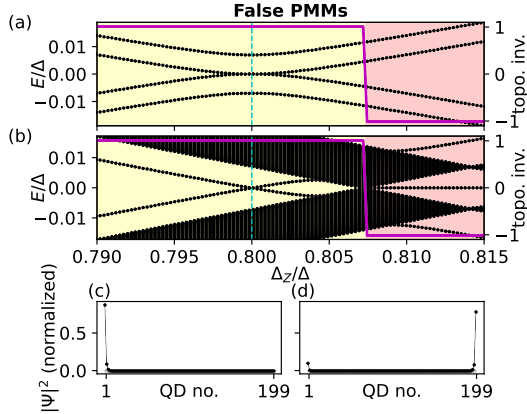


FIG. 12. The parameters are as given in Fig. 1 of the SM, i.e., $t/\Delta = 0.24$, $\Phi_{\text{SOI}} = 0.42\pi$, $U = 0$, $\mu/\Delta = -0.786$, and $\mu_M/\Delta = 3.843$. In (c) and (d) $\Delta_Z/\Delta = 0.8$.

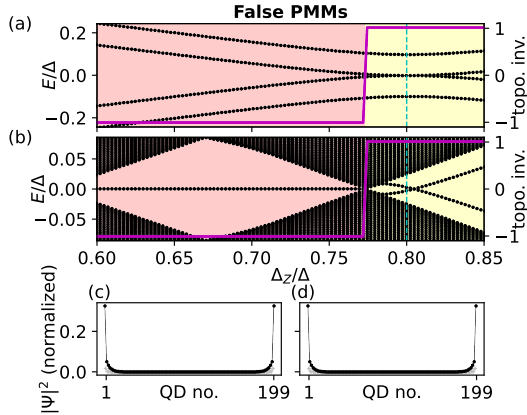


FIG. 13. The parameters are as given in Fig. 2 of the SM, i.e., $t/\Delta = 0.7$, $\Phi_{\text{SOI}} = 0.38\pi$, $U = 0$, $\mu/\Delta = 0.953$, and $\mu_M/\Delta = 3.086$. In (c) and (d) $\Delta_Z/\Delta = 0.8$.

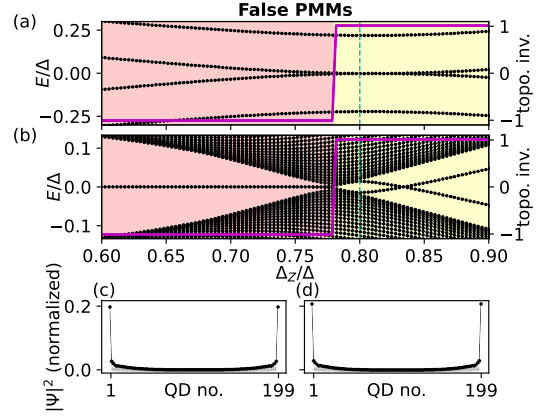


FIG. 14. The parameters are as given in Fig. 3 of the SM, i.e., $t/\Delta = 1.27$, $\Phi_{\text{SOI}} = 0.38\pi$, $U = 0$, $\mu/\Delta = 1.239$, and $\mu_M/\Delta = 4.110$. In (c) and (d) $\Delta_Z/\Delta = 0.8$.

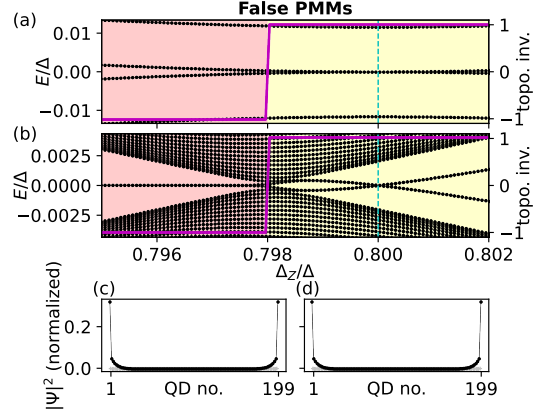


FIG. 15. The parameters are as given in Fig. 4 of the SM, i.e., $t/\Delta = 0.19$, $\Phi_{\text{SOI}} = 0.36\pi$, $U = 0$, $\mu/\Delta = 0.814$, and $\mu_M/\Delta = 2.170$. In (c) and (d) $\Delta_Z/\Delta = 0.8$.

1. DMRG

For a finite on-site Coulomb interaction $U > 0$, one can no longer use the BdG Hamiltonian to calculate the energy spectrum. Instead, the second quantized form of Eq. (1) of the main text must be used. The corresponding Hamiltonian, however, scales exponentially with the number of sites in the system, thus making the long chain limit computationally expensive. We therefore use DMRG [1–3], more specifically, the ITensor library [5], to calculate the energy difference ΔE [defined in Eq. (3) of the main text] as a function of the Zeeman energy Δ_Z , see Fig. 19. This does not allow for a study of the closing and reopening of the bulk gap, or calculating the topological invariant. However, it still gives an idea of whether the corresponding state is related to a topological MBS, or if it is a false PMMs. If it is a true PMMs, then in the long chain limit, the state is at zero energy and there is a finite range of Δ_Z values around it which also exhibits zero-energy states, see Fig. 19(a), which shows a

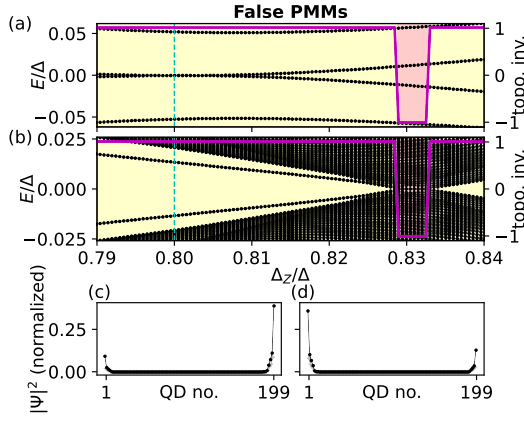


FIG. 16. The parameters are as given in Fig. 5 of the SM, with $t/\Delta = 0.41$, $\Phi_{\text{SOI}} = 0.06\pi$, $U = 0$, $\mu/\Delta = 0.831$, and $\mu_M/\Delta = 0.397$. In (c) and (d) $\Delta_Z/\Delta = 0.8$.

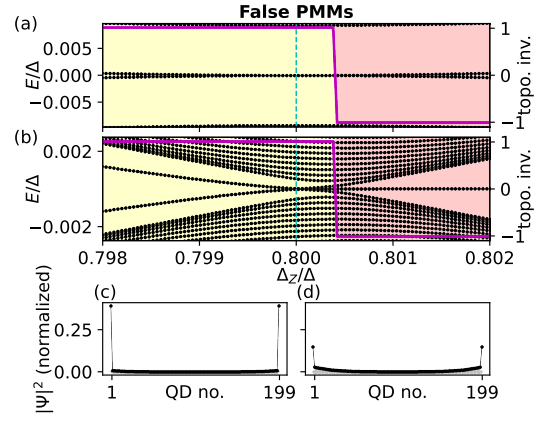


FIG. 18. The parameters are as given in Fig. 7 of the SM, i.e., $t/\Delta = 0.15$, $\Phi_{\text{SOI}} = 0.34\pi$, $U = 0$, $\mu/\Delta = -0.790$ and $\mu_M/\Delta = 1.793$. In (c) and (d) $\Delta_Z/\Delta = 0.8$.

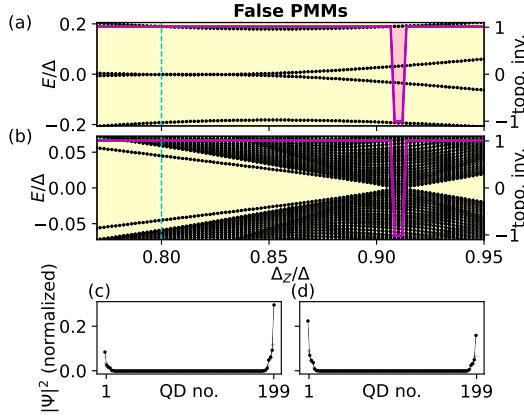


FIG. 17. The parameters are as given in Fig. 6 of the SM, i.e., $t/\Delta = 0.64$, $\Phi_{\text{SOI}} = 0.12\pi$, $U = 0$, $\mu/\Delta = 0.936$, and $\mu_M/\Delta = 0.870$. In (c) and (d) $\Delta_Z/\Delta = 0.8$.

true PMMs. If the state is a false PMMs, then in the long chain limit, the state is either no longer at zero energy, or there is no finite range of Δ_Z values around it which exhibits zero-energy states, see Figs. 19(f)-(h), which show false PMMs.

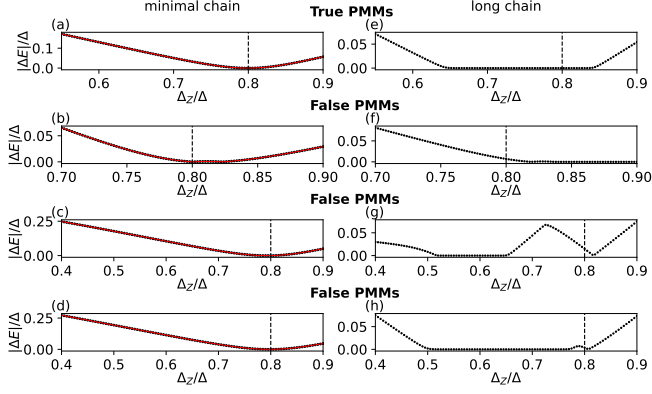


FIG. 19. The energy difference ΔE [defined in Eq. (3) of the main text] between the even and odd ground state, calculated in the minimal chain [(a)-(d), setup as in Fig. 1(a) of the main text] and the long chain limit [(e)-(h), setup as in Fig. 1(b) of the main text, consisting of 101 QDs, 51 of which are normal QDs and 50 are QDs proximitized by a superconductor] using DMRG (black dots) and exact diagonalization in (a)-(d) (red line). For all panels, we are interested in the state at $\Delta_Z/\Delta = 0.8$. In the minimal chain, all four examples have $\Delta E \approx 0$, thus these states are PMMs. In (e), the long chain limit for the first example, the state remains at zero energy and there is a finite range of Δ_Z values around it that also exhibits zero-energy states, thus the state is a true PMM. In contrast, in the long chain limit for the second to fourth examples [panels (f)-(h)], the state is either no longer at zero energy, or there is no finite range of Δ_Z values around it which exhibit zero-energy states. Therefore, these examples show false PMMs. The parameters for (a) and (e) are as for Fig. 8 of the SM: $t/\Delta = 0.4$, $\Phi_{\text{SOI}} = 0.22\pi$, $U/\Delta = 4.69$, $\mu/\Delta = 0.870$, and $\mu_M/\Delta = 0.939$. The parameters for (b) and (f) are as for Fig. 9 of the SM: $t/\Delta = 0.6$, $\Phi_{\text{SOI}} = 0.06\pi$, $U/\Delta = 4.68$, $\mu/\Delta = 0.657$, and $\mu_M/\Delta = -0.0825$. The parameters for (c) and (g) are as for Fig. 10 of the SM: $t/\Delta = 1.29$, $\Phi_{\text{SOI}} = 0.46\pi$, $U/\Delta = 4.31$, $\mu/\Delta = 1.151$, and $\mu_M/\Delta = 4.768$. The parameters for (d) and (h) are as for Fig. 11 of the SM: $t/\Delta = 0.76$, $\Phi_{\text{SOI}} = 0.38\pi$, $U/\Delta = 3.81$, $\mu/\Delta = 1.000$, and $\mu_M/\Delta = 2.515$.

C. Zero-energy conductance

In Figs. 20-26, we present the zero-energy conductance as the chemical potentials μ_L and μ_R are varied independently, for different values of μ_M . Panels (a), (e), and (i) show the local conductance G_{LL} , panels (b), (f), and (j) show the nonlocal conductance G_{LR} , panels (c), (g), and (k) show the nonlocal conductance G_{RL} , and panels (d), (h), and (l) show the local conductance G_{RR} . Furthermore, panels (a)-(d) show the conductance for a chemical potential $\mu_{M,1}$ that is smaller than the value of μ_M at the ROT, panels (e)-(h) show the conductance for $\mu_{M,2}$ in the ROT, and panels (i)-(l) show the conductance for a chemical potential $\mu_{M,3}$ that is larger than the value of μ_M at the ROT. All conductance values are normalized to the maximum conductance value for this parameter set. The conductance is calculated using the Python package Kwant [6], where t_l is the hopping amplitude from the outer QDs to the lead. This hopping is assumed to have no SOI. Since the BdG formulation of the Hamiltonian is used for the calculations, we show only conductance measurements for parameter sets where $U = 0$.

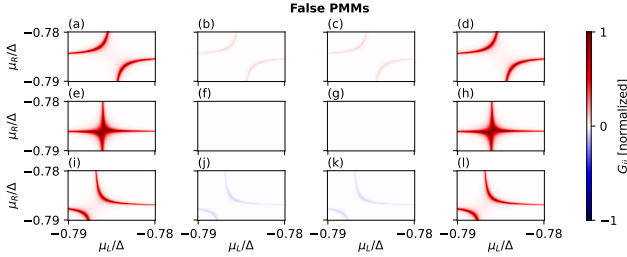


FIG. 20. The parameters are as given in Fig. 1 of the SM, i.e., $t/\Delta = 0.24$, $\Phi_{\text{SOI}} = 0.42\pi$, $U = 0$, and $\Delta_Z/\Delta = 0.8$, $t_l = 5 \cdot 10^{-5}$, $\mu_{M,1}/\Delta = 3.500$, $\mu_{M,2}/\Delta = 3.843$, and $\mu_{M,3}/\Delta = 4.187$.

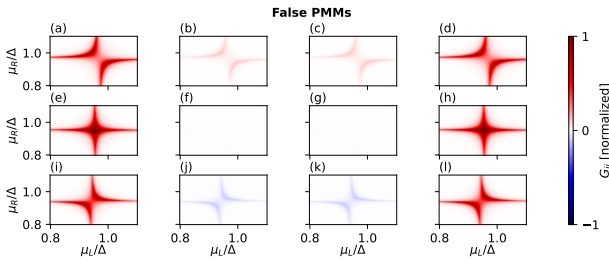


FIG. 21. The parameters are as given in Fig. 2 of the SM, i.e., $t/\Delta = 0.7$, $\Phi_{\text{SOI}} = 0.38\pi$, $U = 0$, $\Delta_Z/\Delta = 0.8$, $t_l = 4 \cdot 10^{-3}$, $\mu_{M,1}/\Delta = 2.793$, $\mu_{M,2}/\Delta = 3.086$, and $\mu_{M,3}/\Delta = 3.379$.

D. Finite-energy conductance, tuning one QD

In Figs. 27-33, we show the conductance at finite energy. All parameters are tuned to the values of the corresponding ROT, then the chemical potential of the left

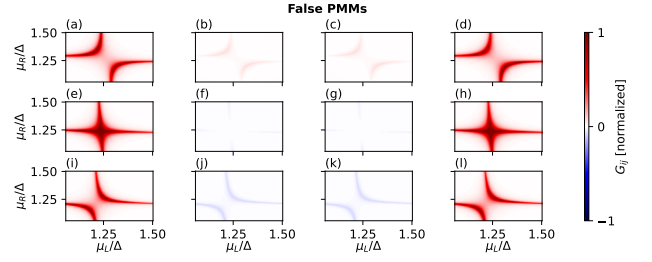


FIG. 22. The parameters are as given in Fig. 3 of the SM, i.e., $t/\Delta = 1.27$, $\Phi_{\text{SOI}} = 0.38\pi$, $U = 0$, $\Delta_Z/\Delta = 0.8$, $t_l = 4 \cdot 10^{-3}$, $\mu_{M,1}/\Delta = 3.888$, $\mu_{M,2}/\Delta = 4.110$, and $\mu_{M,3}/\Delta = 4.333$.

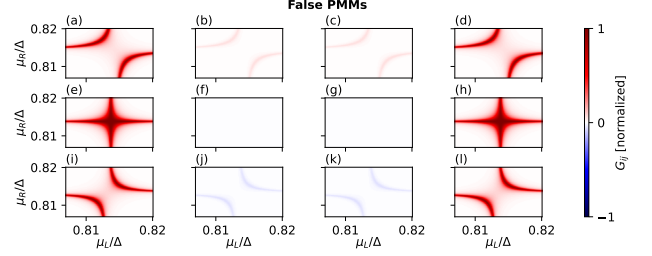


FIG. 23. The parameters are as given in Fig. 4 of the SM, i.e., $t/\Delta = 0.19$, $\Phi_{\text{SOI}} = 0.36\pi$, $U = 0$, $\Delta_Z/\Delta = 0.8$, $t_l = 10^{-4}$, $\mu_{M,1}/\Delta = 2.035$, $\mu_{M,2}/\Delta = 2.170$, and $\mu_{M,3}/\Delta = 2.305$.

QD is tuned away from its ROT value, while the chemical potential of the right QD remains unchanged. This data is used to study excited states. Panels (a) show the local conductance G_{LL} and panels (b) show the nonlocal conductance G_{LR} . All conductance values are normalized to the maximum conductance value for this parameter set.

E. Finite-energy conductance, tuning both QDs

In Figs. 34-42, we show the conductance at finite energy. All parameters are tuned to the values of the corresponding ROT, then the chemical potentials of both QDs are tuned away from the ROT value to $\mu = \mu_L = \mu_R$. Panels (a) show the local conductance G_{LL} and panels (b) show the nonlocal conductance G_{LR} . All conductance values are normalized to the maximum conductance value for this parameter set.

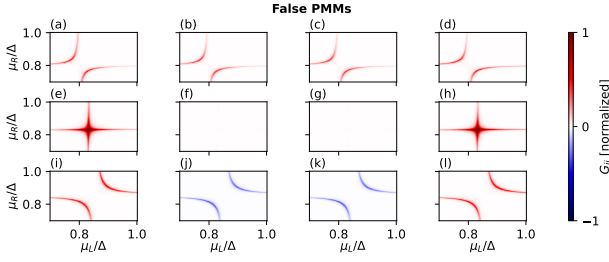


FIG. 24. The parameters are as given in Fig. 5 of the SM, i.e., $t/\Delta = 0.41$, $\Phi_{\text{SOI}} = 0.06\pi$, $U = 0$, $\Delta_Z/\Delta = 0.8$, $t_l = 2 \cdot 10^{-3}$, $\mu_{M,1}/\Delta = 0.199$, $\mu_{M,2}/\Delta = 0.397$, and $\mu_{M,3}/\Delta = 0.596$.

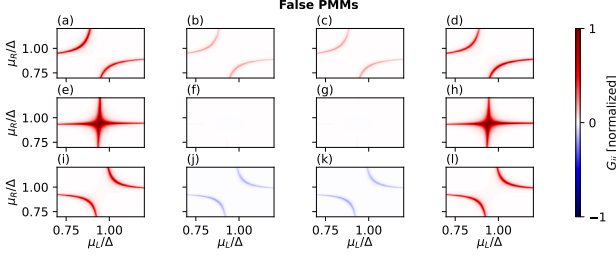


FIG. 25. The parameters are as given in Fig. 6 of the SM, i.e., $t/\Delta = 0.64$, $\Phi_{\text{SOI}} = 0.12\pi$, $U = 0$, and $\Delta_Z/\Delta = 0.8$, $t_l = 3 \cdot 10^{-3}$, $\mu_{M,1}/\Delta = 0.75$, $\mu_{M,2}/\Delta = 0.870$, and $\mu_{M,3}/\Delta = 0.990$.

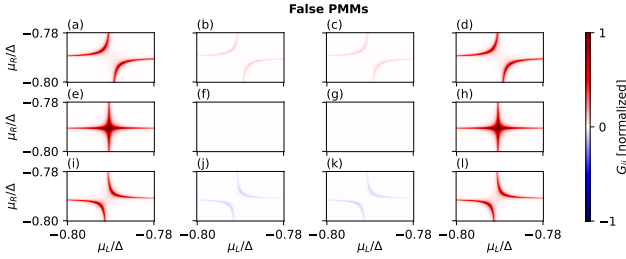


FIG. 26. The parameters are as given in Fig. 7 of the SM, i.e., $t/\Delta = 0.15$, $\Phi_{\text{SOI}} = 0.34\pi$, $U = 0$, $\Delta_Z/\Delta = 0.8$, $t_l = 10^{-4}$, $\mu_{M,1}/\Delta = 1.600$, $\mu_{M,2}/\Delta = 1.793$, and $\mu_{M,3}/\Delta = 1.987$.

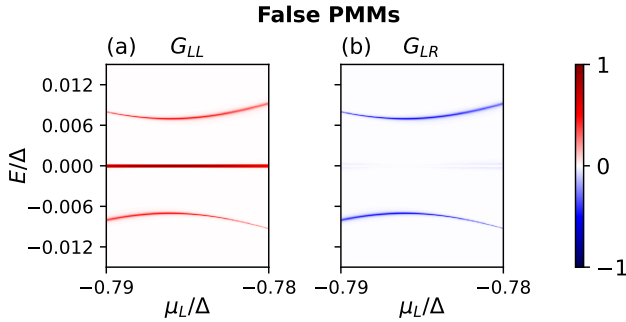


FIG. 27. The parameters are as given in Fig. 1 of the SM, i.e., $t/\Delta = 0.24$, $\Phi_{\text{SOI}} = 0.42\pi$, $U = 0$, and $\Delta_Z/\Delta = 0.8$, $\mu_R/\Delta = -0.786$, $\mu_M/\Delta = 3.843$, and $t_l = 2 \cdot 10^{-4}$.

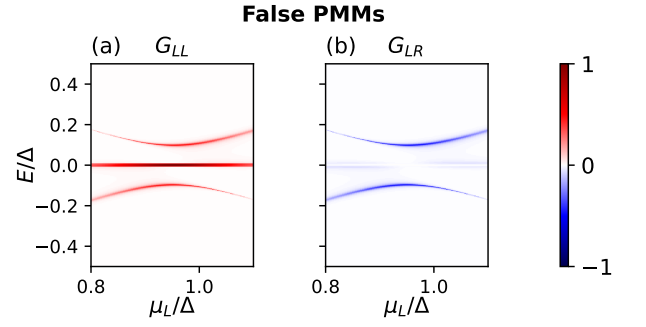


FIG. 28. The parameters are as given in Fig. 2 of the SM, i.e., $t/\Delta = 0.7$, $\Phi_{\text{SOI}} = 0.38\pi$, $U = 0$, $\Delta_Z/\Delta = 0.8$, $\mu_R/\Delta = 0.953$, $\mu_M/\Delta = 3.086$, and $t_l = 8 \cdot 10^{-3}$.

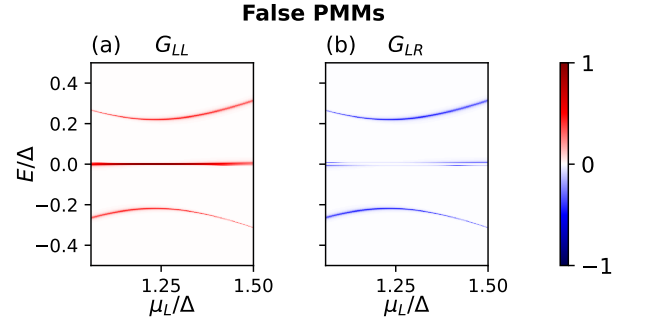


FIG. 29. The parameters are as given in Fig. 3 of the SM, i.e., $t/\Delta = 1.27$, $\Phi_{\text{SOI}} = 0.38\pi$, $U = 0$, $\Delta_Z/\Delta = 0.8$, $\mu_R/\Delta = 1.239$, $\mu_M/\Delta = 4.110$, and $t_l = 6 \cdot 10^{-3}$.

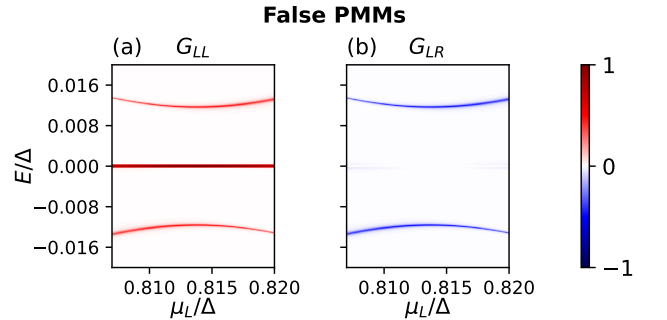


FIG. 30. The parameters are as given in Fig. 4 of the SM, i.e., $t/\Delta = 0.19$, $\Phi_{\text{SOI}} = 0.36\pi$, $U = 0$, $\Delta_Z/\Delta = 0.8$, $\mu_R/\Delta = 0.814$, $\mu_M/\Delta = 2.170$, and $t_l = 3 \cdot 10^{-4}$.

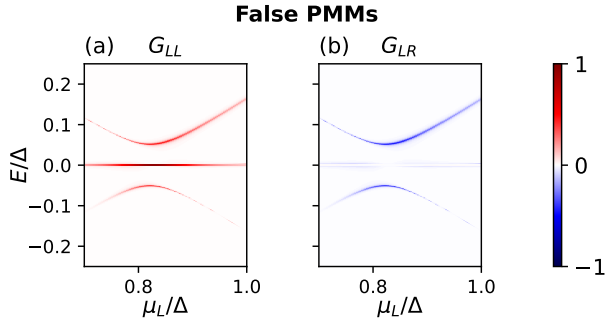


FIG. 31. The parameters are as given in Fig. 5 of the SM, i.e., $t/\Delta = 0.41$, $\Phi_{\text{SOI}} = 0.06\pi$, $U = 0$, $\Delta_Z/\Delta = 0.8$, $\mu_R/\Delta = 0.831$, $\mu_M/\Delta = 0.397$, and $t_l = 3 \cdot 10^{-3}$.

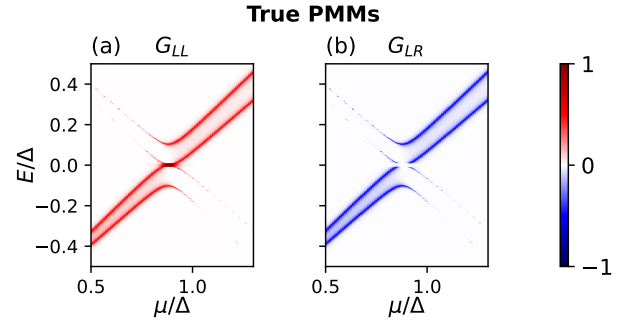


FIG. 34. The parameters are as given in Fig. 5(a)-(b) of the main text, i.e., $t/\Delta = 0.42$, $\Phi_{\text{SOI}} = 0.26\pi$, $U = 0$, $\Delta_Z/\Delta = 0.8$, $\mu_M/\Delta = 1.275$, $t_l/\Delta = 0.01$.

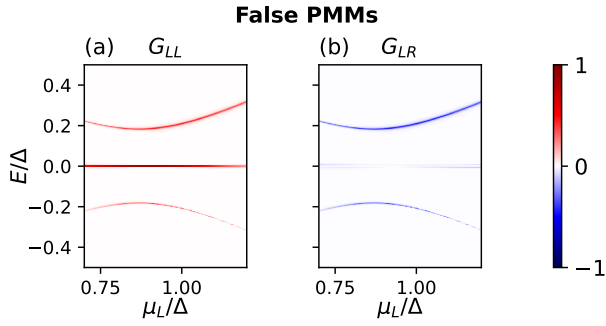


FIG. 32. The parameters are as given in Fig. 6 of the SM, i.e., $t/\Delta = 0.64$, $\Phi_{\text{SOI}} = 0.12\pi$, $U = 0$, and $\Delta_Z/\Delta = 0.8$, $\mu_R/\Delta = 0.936$, $\mu_M/\Delta = 0.870$, and $t_l = 4.5 \cdot 10^{-3}$.

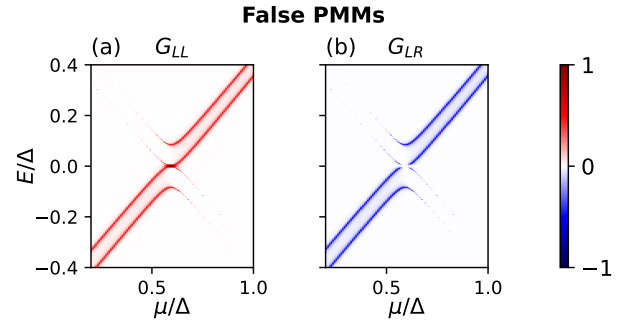


FIG. 35. The parameters are as given in Fig. 5(c)-(d) of the main text, i.e., $t/\Delta = 0.99$, $\Phi_{\text{SOI}} = 0.44\pi$, $U = 0$, $\Delta_Z/\Delta = 0.8$, $\mu_M/\Delta = -3.836$, $t_l/\Delta = 0.006$.

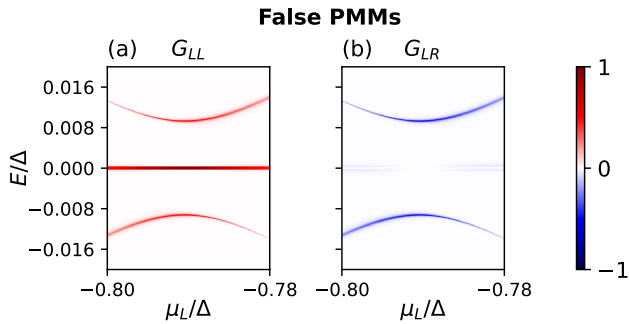


FIG. 33. The parameters are as given in Fig. 7 of the SM, i.e., $t/\Delta = 0.15$, $\Phi_{\text{SOI}} = 0.34\pi$, $U = 0$, $\Delta_Z/\Delta = 0.8$, $\mu_R/\Delta = -0.790$, $\mu_M/\Delta = 1.793$, and $t_l = 3 \cdot 10^{-4}$.

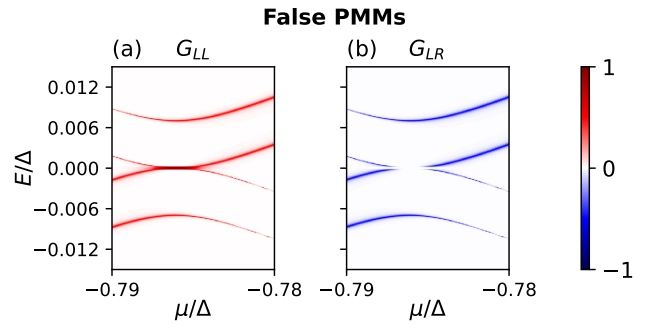


FIG. 36. The parameters are as given in Fig. 1 of the SM, i.e., $t/\Delta = 0.24$, $\Phi_{\text{SOI}} = 0.42\pi$, $U = 0$, and $\Delta_Z/\Delta = 0.8$, $\mu_M/\Delta = 3.843$, $t_l = 2 \cdot 10^{-4}$.

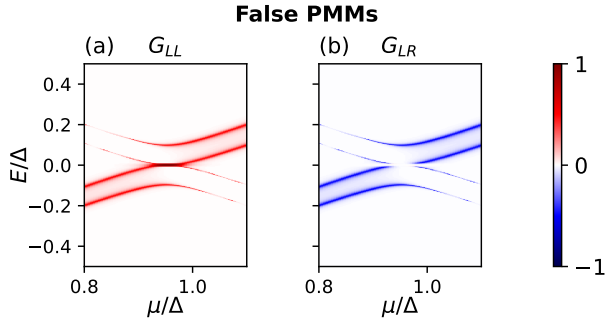


FIG. 37. The parameters are as given in Fig. 2 of the SM, i.e., $t/\Delta = 0.7$, $\Phi_{\text{SOI}} = 0.38\pi$, $U = 0$, $\Delta_Z/\Delta = 0.8$, $\mu_M/\Delta = 3.086$, and $t_l = 8 \cdot 10^{-3}$.

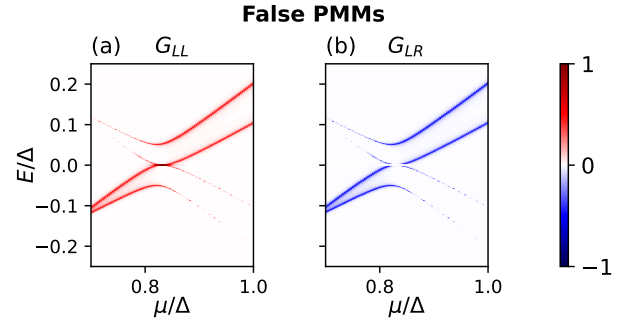


FIG. 40. The parameters are as given in Fig. 5 of the SM, i.e., $t/\Delta = 0.41$, $\Phi_{\text{SOI}} = 0.06\pi$, $U = 0$, $\Delta_Z/\Delta = 0.8$, $\mu_M/\Delta = 0.397$, and $t_l = 3 \cdot 10^{-3}$.

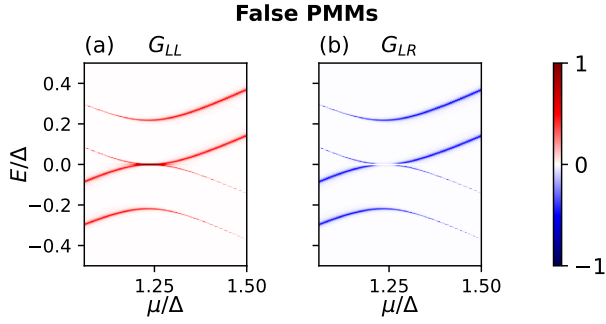


FIG. 38. The parameters are as given in Fig. 3 of the SM, i.e., $t/\Delta = 1.27$, $\Phi_{\text{SOI}} = 0.38\pi$, $U = 0$, $\Delta_Z/\Delta = 0.8$, $\mu_M/\Delta = 4.110$, and $t_l = 6 \cdot 10^{-3}$.

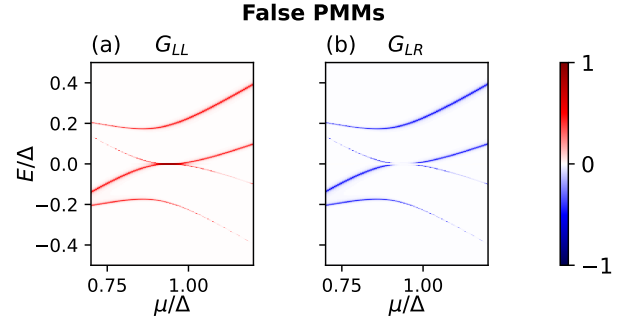


FIG. 41. The parameters are as given in Fig. 6 of the SM, i.e., $t/\Delta = 0.64$, $\Phi_{\text{SOI}} = 0.12\pi$, $U = 0$, and $\Delta_Z/\Delta = 0.8$, $\mu_M/\Delta = 0.870$, and $t_l = 4.5 \cdot 10^{-3}$.

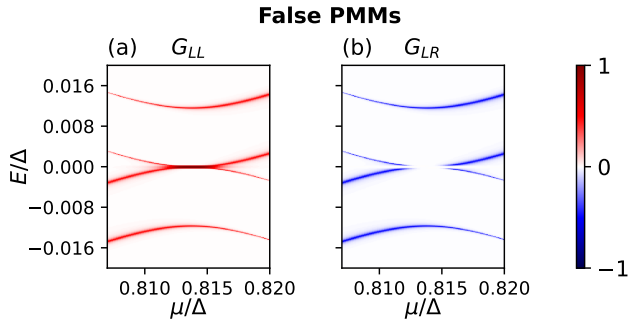


FIG. 39. The parameters are as given in Fig. 4 of the SM, i.e., $t/\Delta = 0.19$, $\Phi_{\text{SOI}} = 0.36\pi$, $U = 0$, $\Delta_Z/\Delta = 0.8$, $\mu_M/\Delta = 2.170$, and $t_l = 3 \cdot 10^{-4}$.

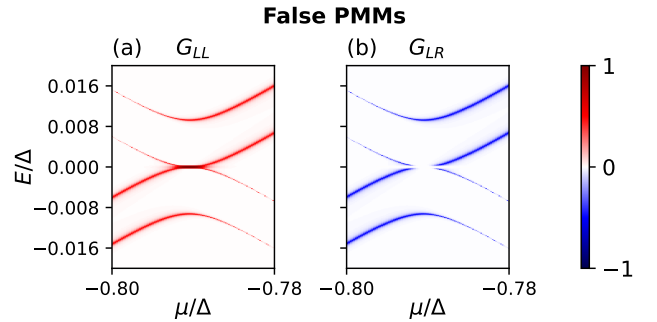


FIG. 42. The parameters are as given in Fig. 7 of the SM, i.e., $t/\Delta = 0.15$, $\Phi_{\text{SOI}} = 0.34\pi$, $U = 0$, $\Delta_Z/\Delta = 0.8$, $\mu_M/\Delta = 1.793$, and $t_l = 3 \cdot 10^{-4}$.

V. ENERGY SPECTRUM AS A FUNCTION OF CHAIN LENGTH

In the case $U = 0$, the system can be described by the BdG formulation of the Hamiltonian given in Eq. (1) of the main text. In this case, the energy spectrum is symmetric around zero energy and we label the energy levels as $\pm E_0, \pm E_1, \pm E_2, \dots$, with $0 \leq E_0 \leq E_1 \leq E_2, \dots$. Analyzing these energy levels as a function of the number of normal sites N (with one superconducting site between two normal sites, i.e., there are $2N - 1$ QDs in total) can help to distinguish between true and false PMMs, see Fig. 43. In both examples shown, E_0 stays at, or close to, zero energy, as expected for MBSs. However, in the case of true PMMs, the first excitation energy, E_1 , tends towards a finite value, whereas for false PMMs, E_1 tends towards E_0 , thus indicating the fourfold degenerate zero-energy states observed for some false PMMs. The second excited energy level, E_2 tends towards E_1 in the case of a true PMMs, whereas it tends towards a finite value away from $E_1 \approx E_0$ for false PMMs. In some cases, a few normal sites are sufficient to distinguish between the two cases, see Fig. 43(b). In other cases, chains with tens of normal sites are required, see Figs. 43(c) and 43(d).

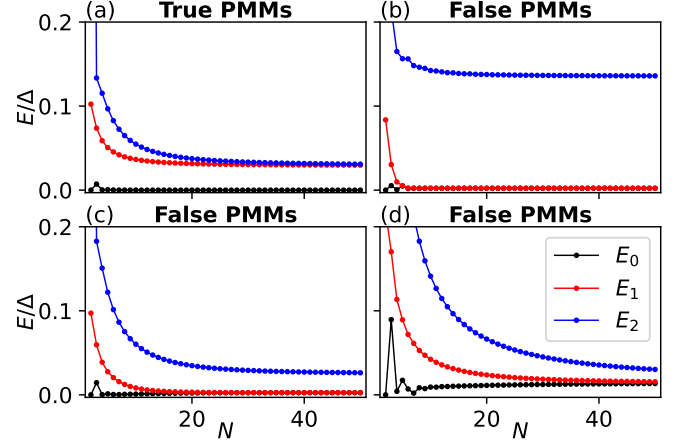


FIG. 43. Energy levels of the BdG formulation of the Hamiltonian given in Eq. (1) of the main text. The spectrum is symmetric around zero energy and the energy levels are labelled as $\pm E_0, \pm E_1, \pm E_2, \dots$, with $0 \leq E_0 \leq E_1 \leq E_2, \dots$. For both true and false PMMs, one finds examples where E_0 stays at, or close to, zero energy as the number of normal sites N increases. The first excited energy level E_1 , however, tends towards a finite value for true PMMs, indicating the topological gap. For false PMMs, E_1 tends towards E_0 as N increases, thus indicating the fourfold degenerate zero-energy states found in association with false PMMs. The second excited energy level E_2 tends towards E_1 for true PMMs and towards a finite value away from E_1 for false PMMs. In some cases, a few sites are sufficient to distinguish the two cases [panel (b)], in other cases [panels (c) and (d)], many sites are required. For (a), the same parameters as for Fig. 3(a) of the main text are used, i.e., $t/\Delta = 0.42$, $\Phi_{\text{SOI}} = 0.26\pi$, $U = 0$, $\mu/\Delta = 0.884$, and $\mu_M/\Delta = 1.275$. For (b), the same parameters as for Fig. 3(e) of the main text are used, i.e., $t/\Delta = 0.99$, $\Phi_{\text{SOI}} = 0.44\pi$, $U = 0$, $\mu/\Delta = 0.592$, and $\mu_M/\Delta = -3.836$. For (c), the same parameters as for Fig. 13 of the SM are used, i.e., $t/\Delta = 0.7$, $\Phi_{\text{SOI}} = 0.38\pi$, $U = 0$, $\mu/\Delta = 0.953$, and $\mu_M/\Delta = 3.086$. For (d), the same parameters as for Fig. 14 of the SM are used, i.e., $t/\Delta = 1.27$, $\Phi_{\text{SOI}} = 0.38\pi$, $U = 0$, $\mu/\Delta = 1.239$, and $\mu_M/\Delta = 4.110$. In all four panels, $\Delta_Z/\Delta = 0.8$.

VI. FALSE PMM EXAMPLES OF CHAINS STARTING AND ENDING WITH A SUPERCONDUCTOR

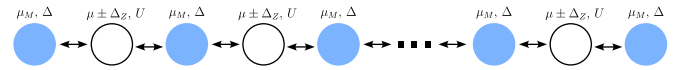


FIG. 44. Slightly adapted long chain limit, where, compared to the setup in Fig. 1(b) of the main text, the chain starts and ends with a superconducting QD. Therefore, each normal QD is now directly coupled to two superconducting QDs.

We have shown that two-fold degenerate energy levels split away from the bulk states because the outer QDs are fundamentally different compared to the QDs in the bulk. This fundamental difference stems from the fact

that the two outer normal QDs are directly coupled to only one superconducting QD, whereas the normal QDs couple to two superconducting QDs. If one adds additional superconducting QDs to the left and right end of the chain (see Fig. 44), it appears that all normal QDs are equivalent, since now each normal QD couples directly to two superconducting QDs. This is, however, not the case because higher-order tunneling terms still distinguish between the QDs at the ends of the chain and in the bulk. Therefore, we still find localised states on these sites with energies that split away from bulk states in the long chain limit.

As was the case for the chains starting and ending with a normal QD, qualitatively, the energy difference, charge difference, and Majorana polarization for a true PMM (Fig. 45) and a false PMM (Fig. 46) do not differ for a chain starting and ending with a superconducting QD. Only the energy spectrum and topological invariant in a long (infinite) chain (Figs. 47 and 48) reveal whether the states are topological or trivial.

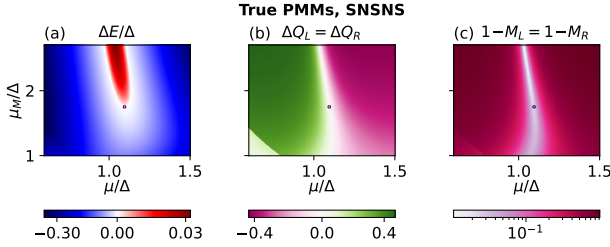


FIG. 45. The parameters are $t/\Delta = 0.6$, $\Phi_{\text{SOI}} = 0.26\pi$, $U = 0$, and $\Delta_Z/\Delta = 0.8$. The threshold values for the ROT are $\Delta E_{\text{th}}/\Delta = 10^{-3}$, $\Delta Q_{\text{th}} = 0.03$, $M_{\text{th}} = 0.03$, and the maximum excitation gap in the ROT is $E_{\text{ex}}/\Delta = 0.153$.

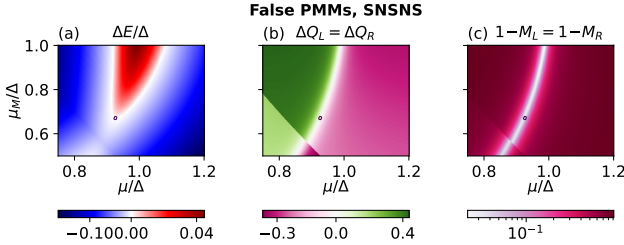


FIG. 46. The parameters are $t/\Delta = 0.5$, $\Phi_{\text{SOI}} = 0.04\pi$, $U = 0$, and $\Delta_Z/\Delta = 0.8$. The threshold values for the ROT are $\Delta E_{\text{th}}/\Delta = 10^{-3}$, $\Delta Q_{\text{th}} = 0.05$, $M_{\text{th}} = 0.05$, and the maximum excitation gap in the ROT is $E_{\text{ex}}/\Delta = 0.041$.

A. Conductance

When calculating the conductance in a long chain that starts and ends with a superconducting QD, one must first decide if the leads are attached to the superconducting QDs, or to the first normal QDs. Figures 47 and 48

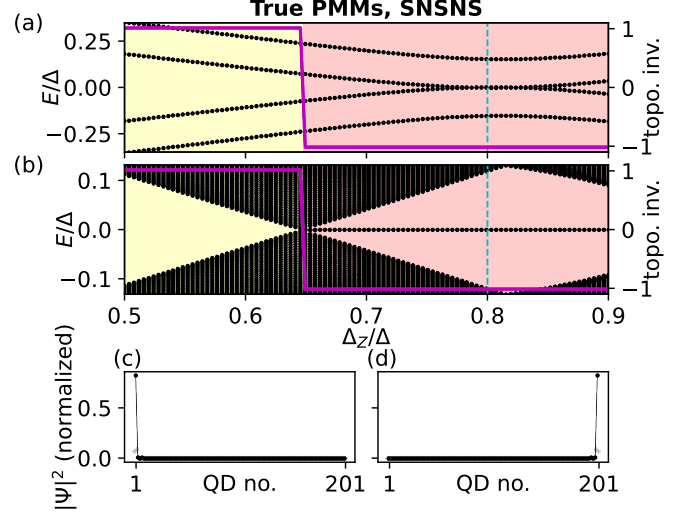


FIG. 47. The parameters are as given in Fig. 45, i.e., $t/\Delta = 0.6$, $\Phi_{\text{SOI}} = 0.26\pi$, $U = 0$, $\mu/\Delta = 1.096$, and $\mu_M/\Delta = 1.771$. We can see that these parameters in the long chain limit result in a topological MBS.

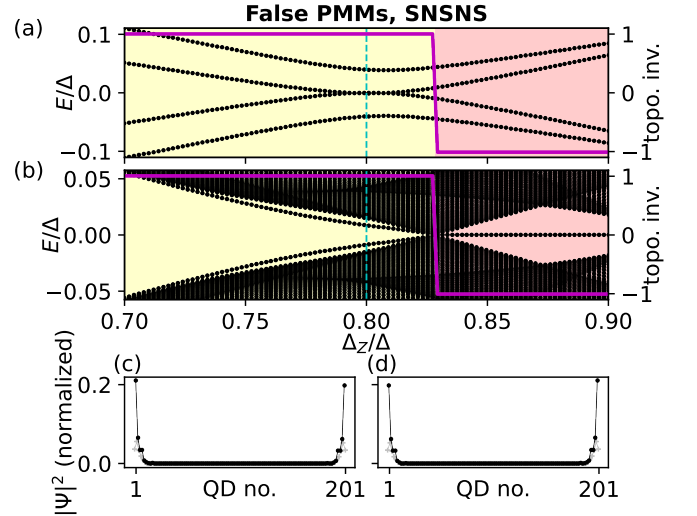


FIG. 48. The parameters are as given in Fig. 46, i.e., $t/\Delta = 0.5$, $\Phi_{\text{SOI}} = 0.04\pi$, $U = 0$, $\mu/\Delta = 0.926$, and $\mu_M/\Delta = 0.674$. We can see that these parameters in the long chain limit do not result in topological MBSs and therefore these states are false PMMs.

show that the zero-energy states are mainly localized on the first normal QDs. Thus, attaching the leads to the outer superconducting QDs adds a further complication to the system, because these superconducting QDs act as insulators between the leads and the probed state. Consequently, we attached the leads to the first normal QDs.

The zero-energy conductance simulations (Figs. 49 and 50) as well as the finite energy conductance simulations where the chemical potential on one QD (Figs. 51 and 52) or on two QDs (Figs. 53 and 54) is tuned away from the ideal ROT value, do not distinguish true PMMs

from false PMMs.

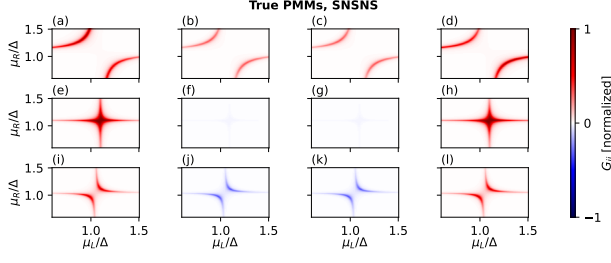


FIG. 49. The parameters are as given in Fig. 45, i.e., $t/\Delta = 0.6$, $\Phi_{\text{SOI}} = 0.26\pi$, $U = 0$, $\Delta_Z/\Delta = 0.8$, $t_l = 10^{-2}$, $\mu_{M,1}/\Delta = 1.000$, $\mu_{M,2}/\Delta = 1.771$, $\mu_{M,3}/\Delta = 2.543$.

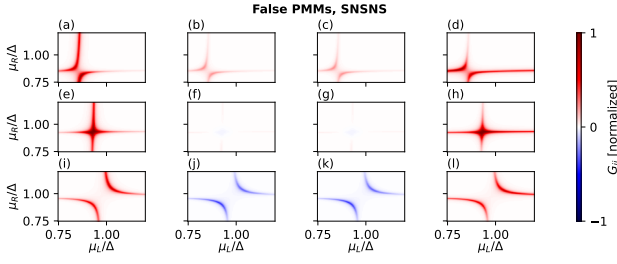


FIG. 50. The parameters are as given in Fig. 46, i.e., $t/\Delta = 0.5$, $\Phi_{\text{SOI}} = 0.04\pi$, $U = 0$, $\Delta_Z/\Delta = 0.8$, $t_l = 5 \cdot 10^{-3}$, $\mu_{M,1}/\Delta = 0.500$, $\mu_{M,2}/\Delta = 0.674$, $\mu_{M,3}/\Delta = 0.848$.

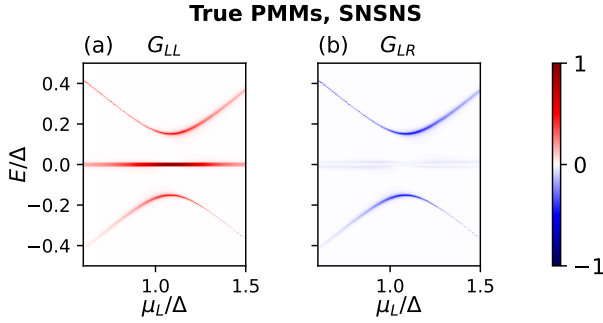


FIG. 51. The parameters are as given in Fig. 45, i.e., $t/\Delta = 0.6$, $\Phi_{\text{SOI}} = 0.26\pi$, $U = 0$, $\Delta_Z/\Delta = 0.8$, $\mu_R/\Delta = 1.096$, $\mu_M/\Delta = 1.771$, and $t_l/\Delta = 0.01$.

False PMMs, SNSNS

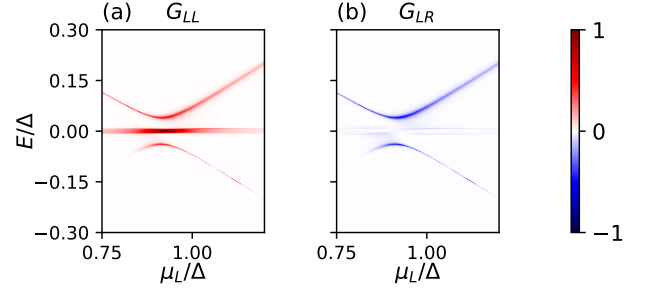


FIG. 52. The parameters are as given in Fig. 46, i.e., $t/\Delta = 0.5$, $\Phi_{\text{SOI}} = 0.04\pi$, $U = 0$, $\Delta_Z/\Delta = 0.8$, $\mu_R/\Delta = 0.926$, $\mu_M/\Delta = 0.674$, and $t_l/\Delta = 7 \cdot 10^{-3}$.

True PMMs, SNSNS

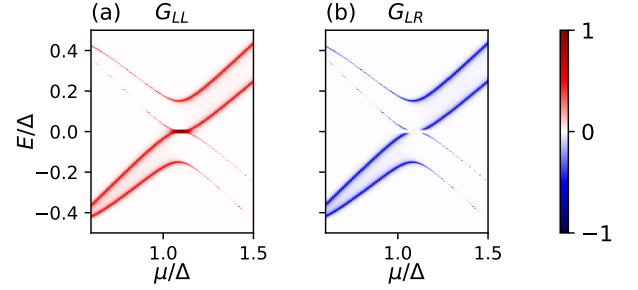


FIG. 53. The parameters are as given in Fig. 45, i.e., $t/\Delta = 0.6$, $\Phi_{\text{SOI}} = 0.26\pi$, $U = 0$, $\Delta_Z/\Delta = 0.8$, $\mu_M/\Delta = 1.771$, and $t_l/\Delta = 0.01$.

False PMMs, SNSNS

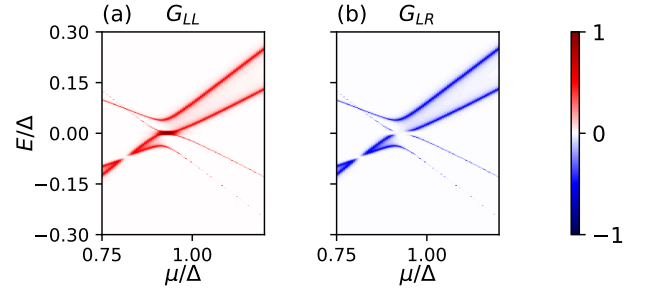


FIG. 54. The parameters are as given in Fig. 46, i.e., $t/\Delta = 0.5$, $\Phi_{\text{SOI}} = 0.04\pi$, $U = 0$, $\Delta_Z/\Delta = 0.8$, $\mu_M/\Delta = 0.674$, and $t_l/\Delta = 7 \cdot 10^{-3}$.

-
- [1] S. R. White, Density matrix formulation for quantum renormalization groups, Phys. Rev. Lett. **69**, 2863 (1992).
 - [2] S. R. White, Density-matrix algorithms for quantum renormalization groups, Phys. Rev. B **48**, 10345 (1993).
 - [3] U. Schollwöck, The density-matrix renormalization group, Rev. Mod. Phys. **77**, 259 (2005).
 - [4] C.-K. Chiu, J. C. Y. Teo, A. P. Schnyder, and S. Ryu, Classification of topological quantum matter with symmetries, Rev. Mod. Phys. **88**, 035005 (2016).
 - [5] M. Fishman, S. R. White, and E. M. Stoudenmire, The ITensor Software Library for Tensor Network Calculations, SciPost Phys. Codebases , 4 (2022).
 - [6] C. W. Groth, M. Wimmer, A. R. Akhmerov, and X. Waintal, Kwant: a software package for quantum transport, New Journal of Physics **16**, 063065 (2014).